

Unconventional criticality, scaling breakdown, and diverse universality classes in the Wilson-Cowan model of neural dynamics

Helena Christina Piuvezam ^{1,*} Bóris Marin ² Mauro Copelli ¹ and Miguel A. Muñoz ^{3,†}

¹*Departamento de Física, Universidade Federal de Pernambuco, Recife PE 50670-901, Brazil*

²*Centro de Matemática, Computação e Cognição, Universidade Federal do ABC, São Bernardo do Campo, Brazil*

³*Instituto Carlos I de Física Teórica y Computacional, Universidad de Granada, Granada, Spain*



(Received 18 January 2023; accepted 4 August 2023; published 11 September 2023)

The Wilson-Cowan model constitutes a paradigmatic approach to understanding the collective dynamics of networks of excitatory and inhibitory units. It has been profusely used in the literature to analyze the possible phases of neural networks at a mean-field level, e.g., assuming large fully connected networks. Moreover, its stochastic counterpart allows one to study fluctuation-induced phenomena, such as avalanches. Here we revisit the stochastic Wilson-Cowan model paying special attention to the possible phase transitions between quiescent and active phases. We unveil eight possible types of such transitions, including continuous ones with scaling behavior belonging to known universality classes—such as directed percolation and tricritical directed percolation—as well as six distinct ones. In particular, we show that under some special circumstances, at a so-called “Hopf tricritical directed percolation” transition, rather unconventional behavior is observed, including the emergence of scaling breakdown. Other transitions are discontinuous and show different types of anomalies in scaling and/or exhibit mixed features of continuous and discontinuous transitions. These results broaden our knowledge of the possible types of critical behavior in networks of excitatory and inhibitory units and are, thus, of relevance to understanding avalanche dynamics in actual neuronal recordings. From a more general perspective, these results help extend the theory of nonequilibrium phase transitions into quiescent or absorbing states.

DOI: [10.1103/PhysRevE.108.034110](https://doi.org/10.1103/PhysRevE.108.034110)

I. INTRODUCTION

A large variety of natural systems exhibit a continuous (second-order) phase transition between an active phase and a quiescent (or absorbing) one where all activity ceases [1–5]. This phase transition is often associated with scaling behavior and is typically described by the *directed percolation* universality class, as originally conjectured by Janssen and Grassberger [6,7]. Actually, directed percolation (DP) is one of the most robust classes of universal critical behavior away from thermal equilibrium [1–5,8], as it describes all possible phase transitions into an absorbing state in the absence of additional symmetries or conservation laws, even for multicomponent systems [1,3–5,9,10]. Moreover, some of the representative models of this class, such as the branching process and the contact process [11,12], have been broadly studied in a large variety of contexts, including countless applications in materials science, turbulence, epidemics, theoretical ecology, social sciences, and neuroscience.

Conversely, under some circumstances, phase transitions into quiescent states occur in a discontinuous (or first-order) rather than continuous manner. This is often the case when higher-order reactions are considered, e.g., where more than one active unit is required to activate the third one [5,13,14]. This situation usually involves a bistable regime with phase coexistence and hysteresis. There are also well-studied systems that include both types of transitions, continuous and

discontinuous, as well as a *tricritical* point with a scaling behavior that differs from DP and is described by the so-called tricritical directed percolation (TDP) universality class (see e.g., a modified contact process [13,15]).

In the context of neuronal systems, the experimental work by Beggs and Plenz reported on the existence of *neuronal avalanches* (i.e., outbursts of neuronal activity between quiescent periods). These exhibited highly variable sizes and durations, which were both distributed as power laws. Moreover, the associated exponents were found to be consistent with those of critical systems in the mean-field DP universality class [16], suggesting that brain dynamics could be poised near the edge of a phase transition [17–22]. Further experimental works reported evidence of scaling exponents deviating from DP [23,24], so that the interpretation of the scaling behavior in terms of universality classes remains a current matter of debate [19]. In particular, the possible departure from the standard DP class (together with the possible existence of discontinuous transitions in brain dynamics [25–27]) raises a number of questions from a theoretical point of view. For example, the fact that neuronal networks include inhibitory units—which hinder activity propagation and are not usually included in simple models in the DP class, such as the standard branching process—triggered a renewed interest in the scrutiny of novel types of phase transitions in networks of excitatory and inhibitory units [28–36]. Do different types of quiescent to active phase transitions emerge in simple models of activity propagation once inhibitory effects are considered?

Here, to further advance our knowledge along these lines, we revisit one of the most broadly studied parsimonious models in neuroscience: the Wilson-Cowan model [37] as

*hcpuvezam@gmail.com

†mamunoz@onsager.ugr.es

well as its stochastic counterpart [28,36]. We systematically analyze the resulting phase diagram, carefully analyzing all the possible phases and phase transitions. In particular, we reveal that, depending on the relative strengths of excitatory and inhibitory couplings, there can be up to eight different types of phase transitions into quiescence. Some of them exhibit well-known scaling behavior (such as DP or TDP), while others are discontinuous or show different types of anomalies in scaling or even mixed features of continuous and discontinuous transitions. Finally, we elucidate a unique type of phase transition that is highly nontrivial, exhibiting unconventional behavior and breakdown of scaling.

Our results help rationalize and categorize the possible types of criticality in networks of excitatory and inhibitory units, contributing to the advance of the brain-criticality hypothesis and of the general theory of nonequilibrium phase transitions [4].

II. THE WILSON-COWAN MODEL AND ITS STOCHASTIC COUNTERPART

In its original formulation, the Wilson-Cowan model describes the collective deterministic (or “mean-field”) behavior of a local population of both excitatory and inhibitory neurons by means of two coupled differential equations [37]. Such equations reproduce—as a function of a set of coupling-strength parameters—a variety of possible dynamical regimes (all of which have counterparts in actual neuronal systems [33,38–40]) that are delimited by phase transitions (bifurcation lines) [41,42].

To go beyond this deterministic or mean-field picture, Benayoun *et al.* [28] proposed a microscopic version of the Wilson-Cowan model in the form of a Markovian process for a population of coupled excitatory and inhibitory individual binary neurons that can be either active or inactive [43]. In the so-called *stochastic Wilson-Cowan* (SWC) model, the state of each unit ℓ at a given time t —which can be either excitatory (E) or inhibitory (I)—is given by $\sigma_\ell^{E/I}(t) = 1$ for active neurons and $\sigma_\ell^{E/I}(t) = 0$ for inactive ones. These discrete state variables change according to a master equation specified by transition rates, which are defined as follows.

Each active neuron, regardless of its type, shifts from the active to the quiescent state, $1 \rightarrow 0$, at a constant decay rate α . The reverse transition (activation), $0 \rightarrow 1$, occurs at rate $\Phi(s^\ell)$, defined as

$$\Phi(s^\ell) = \begin{cases} \tanh(s^\ell), & \text{if } s^\ell > 0 \\ 0, & \text{otherwise} \end{cases}, \quad (1)$$

where the *input* s^ℓ to neuron, ℓ is

$$s^\ell = \sum_m w^{\ell m} \sigma_m + h, \quad (2)$$

$w^{\ell m}$ is the synaptic weight from neuron m to neuron ℓ , and h is a constant external input. Observe that the form of the *response function*, $\Phi(s^\ell)$, in Eq. (1) enforces the nonnega-

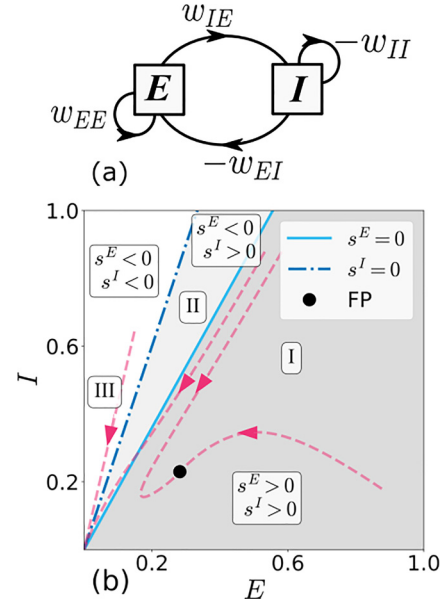


FIG. 1. (a) Sketch of the Wilson-Cowan model, including both excitatory and inhibitory populations and synaptic couplings between them. (b) Owing to the piecewise definition of the response function Φ in Eq. (1), there are three different regions in the state space depending on the total input s on excitatory and inhibitory populations, respectively. In particular, in region I, s^E and s^I are both positive; in region II, s^E is negative and s^I is positive; and, finally, in region III, s^E and s^I are both negative (the figure illustrates these three regions for $w_{EE} = 2.5$, $w_{EI} = 1.5$, $w_{IE} = 1.5$, $w_{II} = 0.5$, and $h = 0$). Observe that when $w_{EE}/w_{EI} > w_{IE}/w_{II}$, the lines $s^E = 0$ and $s^I = 0$ switch position, and region II then shows $s^E > 0$ and $s^I < 0$ (a condition that is not explicitly explored here). The trajectories (red-dashed arrows) show how the system is attracted either to the origin (quiescent state) or to a nontrivial active state or fixed point (FP). As discussed in Sec. IV, initial conditions in region I that are close to the *switching manifold* $s^E = 0$ can cross over to region II. In this case, regions II and III are trapping ones: once trajectories cross the switching manifold, they are unable to return to region I (see Appendix C for a more detailed explanation).

tivity of the transition rates. In what follows, the synaptic weights are chosen to depend only on the type (excitatory or inhibitory) of both the presynaptic and the postsynaptic neuron, leaving [as sketched in Fig. 1(a)] only four free parameters: $w^{\ell m} \in \{w_{EE}, w_{IE}, w_{EI}, w_{II}\} \forall \ell, m$, where, e.g., w_{IE} is the excitatory coupling strength to inhibitory neurons, and so forth. Previous works on this model have often employed symmetric weights—common excitatory ($w_E \equiv w_{EE} = w_{IE}$) and inhibitory ($w_I \equiv w_{II} = w_{EI}$) inputs [28,33,44]—as a way to reduce the dimensionality of the phase diagram. In order to systematically explore the full set of possible phase transitions, here we do not impose such constraints.

This stochastic process can be implemented on different types of networks, as specified by a *connectivity matrix*. As a first approach, one can assume a large fully connected network of size N . Indeed, performing a standard size expansion [45,46], one recovers (up to leading-order) the well-known Wilson-Cowan equations [28] (see Fig. 1)

written as

$$\dot{E} = -\alpha E + (1 - E)\Phi(w_{EE}E - w_{EI}I + h), \quad (3)$$

$$\dot{I} = -\alpha I + (1 - I)\Phi(w_{IE}E - w_{II}I + h), \quad (4)$$

where E and I are the densities of active excitatory and inhibitory neurons, respectively [28] and the coupling constants are defined including a rescaling with the network size. Similarly, by adding next-to-leading corrections, one obtains a set of two Langevin equations which we do not write explicitly here (we just remark that they include square-root noise following the lead of DP and TDP classes [1,3–5]). The pair of coupled stochastic equations allows one to describe fluctuation effects in finite-size (fully connected) networks [28,45,47]. Nevertheless, let us stress that the forthcoming computational analyses refer to simulations of the full microscopic model.

Observe that, owing to the discontinuous derivative of Φ at zero, Eq. (3) and Eq. (4) are piecewise smooth differential equations [48–50]—i.e., they are smooth everywhere except at *switching manifolds*, which are defined by the conditions of vanishing input in the response function in the previous equations: $s^E \equiv w_{EE}E - w_{EI}I + h = 0$ and $s^I \equiv w_{IE}E - w_{II}I + h = 0$. These two conditions divide the state space into three *regions*: I, II, and III, as illustrated in Fig. 1(b) (for $h = 0$):

(1) In region II, the input to excitatory populations is negative, so that Eq. (3) becomes $\dot{E} = -\alpha E$ and trajectories in this region decay exponentially fast to the quiescent phase (either crossing to region III or not; see Appendix C for a more detailed explanation).

(2) Similarly, in region III, the input to both excitatory and inhibitory populations is negative, so that $\dot{E} = -\alpha E$ and $\dot{I} = -\alpha I$, leading to an even faster decay to quiescence.

(3) Conversely, in region I, the total input does not vanish for either subpopulation and the dynamics can be more complex, possibly reaching nontrivial (active) fixed points.

Inspection of Eq. (3) and Eq. (4) readily reveals that trajectories starting in regions II and III do not cross over to region I (as excitation always diminishes in these regimes), but the opposite can happen (see, e.g., the central trajectory shown in Fig. 1 as well as Appendix C).

In the next sections, we explore in detail, both analytically and numerically, the features of each of the possible phase diagrams as well as all the possible phase transitions between quiescent and active states.

III. MEAN-FIELD PHASE DIAGRAMS: GENERAL AND SPECIFIC FEATURES

To avoid confusion, let us first underline that in what follows we refer indistinctly to *phase transitions* or to *bifurcations*, as the present focus is on the description of fully connected networks (i.e., mean-field systems). Thereby, DP transitions correspond to transcritical bifurcations, discontinuous transitions to saddle-node bifurcations, tricritical points to saddle-node-transcritical (codimension-2) bifurcations [51,52], and so forth.

In the absence of any external driving force ($h = 0$), the steady-state conditions for Eq. (3) and Eq. (4) always admit a trivial solution $E^* = I^* = 0$, which defines the *quiescent*

phase as well as, possibly, some nontrivial solutions ($E^* > 0$ and $I^* > 0$) of the following equations:

$$E^* = \frac{1}{w_{IE}} \left[w_{II}I^* + \Phi^{-1} \left(\frac{\alpha I^*}{1 - I^*} \right) \right], \quad (5)$$

$$I^* = \frac{1}{w_{EI}} \left[w_{EE}E^* - \Phi^{-1} \left(\frac{\alpha E^*}{1 - E^*} \right) \right], \quad (6)$$

which define the *active phase*. Observe that Eq. (5) and Eq. (6) are well-defined only as long as Φ^{-1} exists, i.e., in region I [Fig. 1(b)], so that nontrivial solutions exist only inside said region.

In what follows, we analyze the overall phase diagram, describing the stable phases as a function of the model parameters. In particular, without loss of generality, we keep the activity-decay rate $\alpha \neq 0$ and the self-inhibition weight $w_{II} \geq 0$ fixed. Choosing w_{EE} and w_{EI} as control parameters, the system may display three qualitatively different types of phase diagrams in the (w_{EE}, w_{EI}) plane depending on the value of the remaining free parameter, w_{IE} , as illustrated in Fig. 3. Other parameter choices are possible, but the system is always described by one of these three qualitatively different types of phase diagrams.

A. Quiescent phase and its stability limits

First of all, let us stress that the quiescent state is always stable (and is the only stable state) with respect to the introduction of *inhibition-dominated* perturbations (i.e., for initial conditions in regions II and III); in other words, activation of inhibitory neurons does not allow the system to escape from the quiescent state. Therefore, in what follows, we focus on its stability and the resulting phase diagram as a result of *excitation-dominated* perturbations.

Importantly, there are two different types of quiescent phases: The first one is a standard quiescent phase, i.e., a regime in which the quiescent phase is locally stable to excitation-dominated perturbations [Fig. 2(a)]. This occurs if the eigenvalues of the associated stability matrix, as specified by

$$\lambda_{\pm} = \frac{w_{EE} - 2\alpha - w_{II} \pm \sqrt{(w_{EE} + w_{II})^2 - 4w_{EI}w_{IE}}}{2}, \quad (7)$$

have negative real parts (white zone in the diagrams of Fig. 3).

Alternatively, if the eigenvalues have positive real parts and an imaginary component, then, in principle, one could expect oscillations away from quiescence to emerge. However, given the nonsmooth piecewise dynamics, the resulting “curvy” trajectories end up crossing over to region II, where the dynamics follow the equation $\dot{E} = -\alpha E$ and the quiescent state is the only attractor. Therefore, in this regime, small excitatory perturbations to the quiescent state may give rise to large trajectories in state space before returning to quiescence (see Fig. 2(b) and [28,36]). This property is called “excitability” [53] (or “reactivity” [54]) and the corresponding quiescent state is called “excitable quiescent.” Observe that, inside the excitable quiescent phase, there is a region where the eigenvalues are both real and positive. The trajectories continue to fall into regions II and/or III, therefore, the phase remains the same. When in the standard quiescent phase, the

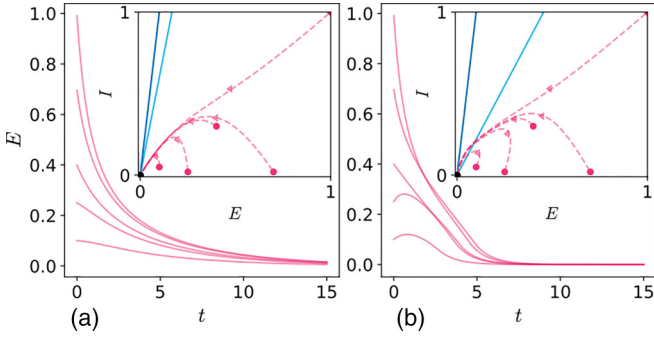


FIG. 2. Two different types of quiescent phases. Time series towards the absorbing state of trajectories (a) on the standard quiescent phase ($w_{EE} = 1.2$ and $w_{IE} = 0.2$) and (b) on the excitable quiescent phase ($w_{EE} = 2.2$ and $w_{IE} = 1.0$). Observe the nonmonotonicity in the second case, which is a manifestation of the excitability of the quiescent state: perturbations can be amplified before trajectories finally decay to quiescence. The insets show the phase space for these two cases, respectively, as well as the corresponding switching manifolds and some sample trajectories (arrows). In the second case, trajectories cross the switching manifold. Parameter values are $\alpha = 1.0$, $w_{II} = 0.2$, and $w_{EI} = 2.0$.

quiescent state loses its local stability when the real part of the largest eigenvalue becomes positive. First, considering a real eigenvalue, it occurs at

$$w_{EE}^T = \alpha + \frac{w_{EI}w_{IE}}{\alpha + w_{II}} \quad (8)$$

as can be easily seen from Eq. (7); note that this condition corresponds to the diagonal blue dashed line in all the plots in

Fig. 3, representing a line of transcritical bifurcations (as well as its continuation to the right).

Not surprisingly, separating the previous two phases (standard quiescent and excitable quiescent), there is a line of (supercritical) Hopf bifurcations (dot-dashed vertical lines in Fig. 3) occurring at

$$w_{EE}^H = 2\alpha + w_{II}, \quad (9)$$

which exist only when there is a nonvanishing imaginary part, i.e., from Eq. (7), at

$$(w_{EE} + w_{II})^2 - 4w_{EI}w_{IE} < 0, \quad (10)$$

so that the Hopf bifurcation is defined only above the Hopf-transcritical point, i.e., above the diagonal blue line in all the phase diagrams in Fig. 3.

Summing up, there are two types of quiescent phases, separated by a line of Hopf bifurcations:

(1) A *standard quiescent phase*, which is represented by a locally stable fixed point (upper left regions in Fig. 3)

(2) An *excitable quiescent phase*, in which local stability is lost, but the origin remains globally stable because the trajectories cross to trapping regions (upper right regions in Fig. 3).

Finally, let us note that the excitable-quiescent state may lose its *global* stability (in favor of a nontrivial active state, as described below) at a transition line that needs to be numerically determined (black dashed line in Fig. 3), beyond which trajectories flow to the alternative active state.

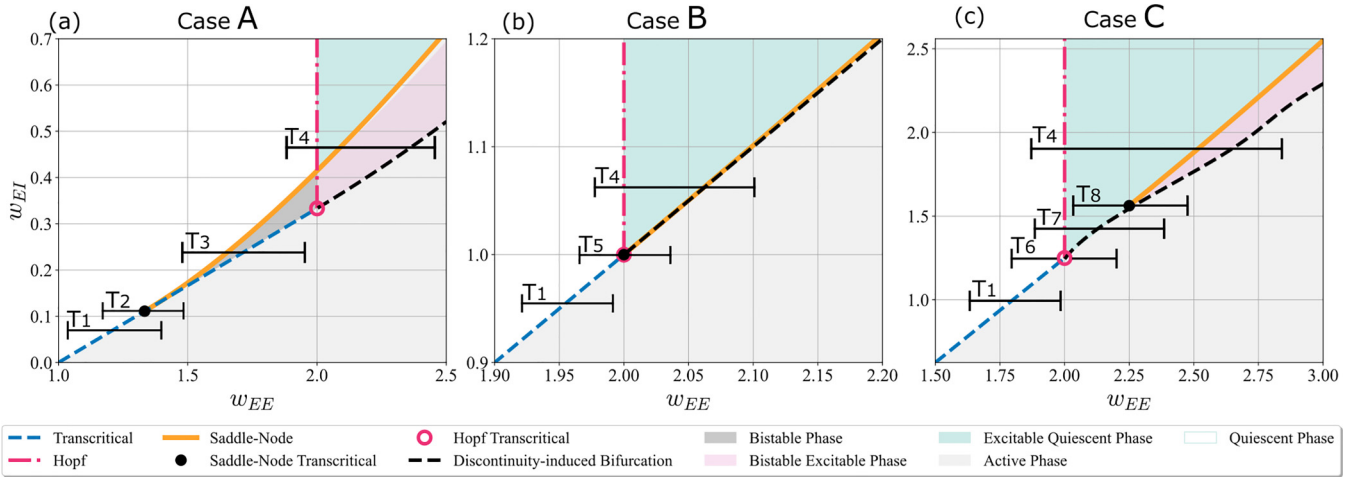


FIG. 3. Different phase diagrams of the model [Eq. (3) and Eq. (4)], with excitation-dominated initial conditions and parameter values: $\alpha = 1$, $w_{II} = 0$, and $w_{IE} = 3$ (Case A), $w_{IE} = 1$ (Case B), and $w_{IE} = 0.8$ (Case C). In all cases, the (vertical dot-dashed) line of Hopf bifurcations separates the standard quiescent phase from the excitable quiescent one. (a) In case A, the Hopf line collides with the (blue dashed) transcritical line to the right of the tricritical point (black dot), within a region of bistability. (c) In case C, on the contrary, the intersection of the Hopf line with the diagonal line occurs to the left of the tricritical point. (b) Between the previous two cases, case B (for which fine-tuning a third parameter, $w_{IE} = 1$, is needed) the Hopf line collides with the transcritical one at a codimension 3 bifurcation point that we call Hopf-tricritical point [Hopf saddle-node-transcritical bifurcation that corresponds to, as we called it, the Hopf tricritical directed percolation ($H+TDP$) point]. In all cases, the standard quiescent phase loses its stability at a line of transcritical bifurcations (blue dashed lines), while the excitable phase loses its global stability from below (i.e., as w_{EI} decreases) at the black dashed line—that may be very close to (or coincide with) the (orange) line of saddle-node bifurcations. Finally, the horizontal black segments T_1, \dots, T_8 represent eight qualitatively different ways to transition from a quiescent to an active state as the control parameter, w_{EE} , increases.

B. Active phase and its stability limits

The active state or phase (with $E^* \neq 0$ and $I^* \neq 0$) becomes a stable solution either at (1) a transcritical bifurcation (i.e., it emerges continuously once the quiescent phase loses its stability in a DP transition), which occurs at Eq. (8) as represented by the blue dashed lines in Fig. 3; (2) a saddle-node (SN) bifurcation, i.e., emerging discontinuously (orange solid line in Fig. 3) at

$$w_{EE}^{SN} = \min_{E^*} \left[\frac{w_{EI} I^*(E^*)}{E^*} + \frac{1}{E^*} \Phi^{-1} \left(\frac{\alpha E^*}{1 - E^*} \right) \right], \quad (11)$$

where E^* and I^* are solutions of Eq. (5) and Eq. (6) that can be solved numerically; or (3) at a tricritical point, where (if) the previous two lines meet (black dot in Fig. 3), to which one can also refer as “saddle-node-transcritical” (SNT) point [its location (w_{EE}^{SNT} , w_{EI}^{SNT}) in the phase diagram is explicitly derived in Appendix B; see, in particular, Eq. (B3) and Eq. (B4)].

Let us emphasize that, even if for the naked eye, the saddle-node (orange) curve in all the plots in Fig. 3 seems to be a continuation of the transcritical (blue dashed) line, parallel to it, that is not exactly the case; the mathematical conditions for both are different.

C. Relative location of the line of Hopf bifurcations

Observe that the line of Hopf bifurcations—which as shown in Fig. 3(a) is always vertical in the (w_{EE} , w_{EI}) plane—collides with the line of transcritical bifurcations at a special point [here named, in general, Hopf-transcritical (HT) bifurcation, which is marked with an empty circle in the different panels of Fig. 3]. From Eq. (8) and Eq. (9), one can easily derive the conditions for the HT point:

$$w_{EI}^{HT} = \frac{(\alpha + w_{II})^2}{w_{IE}}, \quad (12)$$

$$w_{EE}^{HT} = 2\alpha + w_{II}. \quad (13)$$

The key aspect distinguishing the three possible topologies of the phase diagram (A/B/C in Fig. 3) is whether this HT point lies to the right (case A), left (case C), or on top of the tricritical (SNT) point (case B) in phase space:

- (1) Case A: $w_{EE}^{SNT} < w_{EE}^{HT}$,
- (2) Case B: $w_{EE}^{SNT} = w_{EE}^{HT}$,
- (3) Case C: $w_{EE}^{SNT} > w_{EE}^{HT}$.

As already mentioned, these three possibilities are illustrated in Fig. 3, in which the value of w_{IE} is changed (from 3, to 1, and 0.8) to switch between regimes. Also, note that case B requires a higher level of fine-tuning than the other two cases, which appear in broad regions of parameter space. From here on, one needs to separately discuss the three aforementioned possible structures of the phase diagram and carefully classify the diverse types of phase transition emerging in each of them.

1. Case A: Left panel in Fig. 3

In this case, the HT point lies to the right of the tricritical point. Visual inspection of Fig. 3(a) reveals that there are four different ways to go from a quiescent phase (either standard or excitable) to the active one. These are labeled as: T_1 , for

the transcritical bifurcation from the standard quiescent; T_2 , for a standard tricritical transition; T_3 , for a transition through a bistable regime (saddle-node bifurcation with coexistence between the standard quiescent and the active phase); and T_4 , also for a discontinuous transition with bistability, although in this case, between the excitable quiescent phase and the active one.

2. Case B: Central panel in Fig. 3

Here the HT point lies exactly on top of the tricritical point. This structure leads to only three possible types of transitions: T_1 and T_4 (as described above), and a transition labeled T_5 , which occurs through the tricritical (SNT) point that coincides with the special HT point in a codimension 3 bifurcation corresponding to a transition that we call *Hopf tricritical directed percolation (H+TDP) transition*.

3. Case C: Right panel in Fig. 3

In case C, the HT point lies to the left of the tricritical point and there are five types of transitions, including the standard transcritical (T_1) and saddle-node (T_4) ones, as well as three unique ones: T_6 , a transition through the special HT point; T_7 , a transcritical bifurcation but into the excitable quiescent phase; and, finally, T_8 , a tricritical (or SNT) transition into the excitable quiescent phase.

In the next section, we analyze these eight types of phase transitions (or bifurcations)—from T_1 to T_8 —scrutinizing the corresponding peculiarities for each of them.

IV. SCALING PROPERTIES AT THE DIFFERENT TYPES OF TRANSITIONS

Standard linear stability analysis of the fixed points of the (mean-field) dynamics [Eq. (3) and Eq. (4)] allows one to study the nature of bifurcations and make analytical predictions for the scaling behavior [1,4,55]. In particular, a linear approximation of Eq. (5) around the quiescent solution yields a value of I^* proportional to the density of active excitatory neurons E^* , hence in what follows we employ indistinctly either the latter or the sum of both as an order parameter.

In all cases, and for all possible types of transitions, we compute the usual quantities and scaling exponents (as long as they are well defined) customarily employed in the analysis of quiescent-active phase transitions. Even if, generally, three independent exponent values suffice to fully determine the universality class [55,56], here, for the sake of completeness, we determine a larger number of them, which also allows us to check for consistency. In particular, we compute the following:

“*Static exponents*” such as: (1) β , the control parameter one ($E^* \propto \Delta^\beta$), where $\Delta = w_{EE} - w_{EE}^*$ is the distance to the transition point and w_{EE}^* stands, generically, for the value of w_{EE} at the specified bifurcation and (2) δ_h , defined by $E^* \propto h^{1/\delta_h}$, representing the response to a constant external field h at criticality.

“*Correlation exponents*” (ν) such as: the one for (3) the correlation length, ξ_\perp , $\xi_\perp \propto \Delta^{\nu_\perp}$, and for (4) the correlation time, ξ_\parallel , $\xi_\parallel \propto \Delta^{\nu_\parallel}$.

“Dynamic exponents” such as: (5) θ , that governs the time decay of the order parameter $E(t) \propto t^{-\theta}$.

“Spreading exponents” such as those describing: (6) the total number of active sites, $N(t) \propto t^\eta$; (7) the mean-squared radius in surviving runs $R^2(t) \propto t^z$; and (8) the survival probability $P_s(t) \propto t^{-\delta}$ [1].

“Avalanche exponents” defined by: (9) $P(S) \sim S^{-\tau}$, for the distribution of avalanche sizes, S ; (10) $P(T) \sim T^{-\tau}$, for durations, T ; and (11) $S \sim T^\gamma$ linking durations with averaged sizes, $S(T)$.

Note that these last exponents (the spreading and avalanche ones) are not independent of each other, but related through scaling relations as derived in, e.g., [55]

$$\tau = \frac{1 + \eta + 2\delta}{1 + \eta + \delta}, \quad (14)$$

$$\tau_t = 1 + \delta, \quad (15)$$

$$\gamma = \frac{\tau_t - 1}{\tau - 1} = 1 + \delta + \eta, \quad (16)$$

where the last one describes the “crackling noise” scaling relation [57]. Other scaling relations can be found in [4,5,55], in particular,

$$\theta = \beta/\nu_\parallel, \quad (17)$$

relates static and dynamic exponents. Importantly, for standard processes with absorbing states (e.g., DP and TDP), the averaged shape of avalanches with different durations and sizes (or “mean temporal profile of avalanches”) collapses onto a universal curve that typically has a symmetric inverted parabolic form (see Sec. V) [58,59].

It is noteworthy that there is a set of exponents that can be argued to remain unchanged across transition types (a fact that is also confirmed numerically [60]). This is due to the mean-field and diffusive character shared by all the transitions discussed here. In particular, owing to the diffusive nature of the system in all continuous transitions, correlations (ξ) should diverge at the critical point with the well-known mean-field exponents [1,4,5] as follows: $\xi_\perp \propto \Delta^{\nu_\perp}$ with $\nu_\perp = 1/2$, for the correlation length; and $\xi_\parallel \propto \Delta^{\nu_\parallel}$ with $\nu_\parallel = 1$, for the time correlation. From this, given that [55] $z = 2\nu_\perp/\nu_\parallel = 1$, $z = 1$ for all continuous transitions here. Similarly, the survival probability exponent (whose scaling behavior was determined in [61]) always takes a value $\delta = 1$ for all the continuous transitions studied here, implying that $\tau_t = 2$ [see Eq. (15)] is conserved across transitions. Finally, the exponent η is expected to vanish for all mean-field transitions (for which there is no “anomalous dimension” [3]). However, remarkably, here we report on a possible exception to this general rule ($\eta = 2$) for some of the “anomalous” transitions (see below).

Finally, it is worth stressing that many aspects of the transitions, especially those related to discontinuous or hybrid-type transitions, are not expected to exhibit universal features.

A. T_1 : Directed percolation (transcritical bifurcation)

T_1 corresponds to a transcritical bifurcation, describing a continuous transition between the standard quiescent and active phases. As discussed in Sec. I, guided by universality

principles, one expects it to lie in the usual (mean-field) directed percolation universality class (DP) [1,3,4,6,7]. Indeed, this is the case, as explicitly shown in what follows.

Transcritical bifurcations occur when the quiescent steady state loses its local stability, i.e., Eq. (8). Expanding Eq. (3) and Eq. (4) in power series of E^* and I^* , one finds

$$E^*(\Delta; h = 0) = \frac{(\alpha + w_{II})^3}{(\alpha + w_{II})^3 - w_{EI}w_{IE}^2} \Delta + O(\Delta^2), \quad (18)$$

from which $\beta = 1$ follows (see Fig. 4). The introduction of an external field h smooths out the transition [as illustrated with dashed lines in Fig. 4(a)]. Hence, expanding the fixed point in powers of h , at $\Delta = 0$, yields

$$E^*(h; \Delta = 0) = \sqrt{\frac{(\alpha + w_{II})^2(w_{EI} - \alpha)h}{\alpha[w_{IE}w_{EI}^2 - (w_{II} + \alpha)^3]}} + O(h), \quad (19)$$

so that $\delta_h = 2$ [see Fig. 5(a)].

Similarly, one can derive the solution for $I(t)$ and, by expanding it in a power series, obtain $I(t) \approx [w_{IE}/(w_{II} + \alpha)]E(t)$. It is, thus, convenient to define two new variables: Σ and Λ , as the weighted linear combinations:

$$2\Sigma = w_{IE} E + (w_{II} + \alpha)I, \quad (20)$$

$$2\Lambda = w_{IE} E - (w_{II} + \alpha)I, \quad (21)$$

in terms of which the mean-field dynamics [Eq. (3) and Eq. (4)] take a simpler form:

$$2\dot{\Sigma} \approx \Delta\Sigma + (2w_{EE} + 2w_{II} + \Delta)\Lambda + O, \quad (22)$$

$$2\dot{\Lambda} \approx \Delta\Sigma - [2(w_{EE} + w_{II} - 2\alpha) + \Delta]\Lambda + O, \quad (23)$$

where $O = O(\Sigma^2, \Lambda^2, \Sigma\Lambda, \dots)$ stands for higher-order terms. Observe that, right at the transition ($\Delta = 0$), the stability matrix around the origin is

$$A = \begin{pmatrix} 0 & w_{EE}^T + w_{II} \\ 0 & w_{EE}^T - w_{II} - 2\alpha \end{pmatrix}, \quad (24)$$

which has a vanishing eigenvalue, while the second one is strictly negative at criticality for T_1 transitions. This means that Λ decays exponentially fast; therefore, it is an *irrelevant* field for scaling. Only one “slow mode” or “relevant field” exists, Σ , and—as theoretically predicted in Grinstein *et al.* [10] for these conditions—the scaling behavior should coincide with standard DP.

In particular, at the transition point—where the linear term of Eq. (22) vanishes—the quadratic term dominates and therefore $\Sigma(t) \propto t^{-1}$, so that $\theta = 1$ [as numerically confirmed in Fig. 6(a)]. Considering the previous three independent exponent values, one can already conclude that the T_1 transition actually belongs in the DP universality class (see Table I). Nevertheless, for the sake of completeness, the survival probability and the total number of particles, at $\Delta = 0$, are numerically verified to scale with spreading-exponent values $\delta = 1$ [Fig. 7(a)] and $\eta = 0$ [Fig. 8(a)], respectively, as expected for the DP class. We have also confirmed the consistency with DP by numerically analyzing the statistics of avalanches at the transition, revealing exponent values compatible with the DP predictions $\tau = 3/2$,

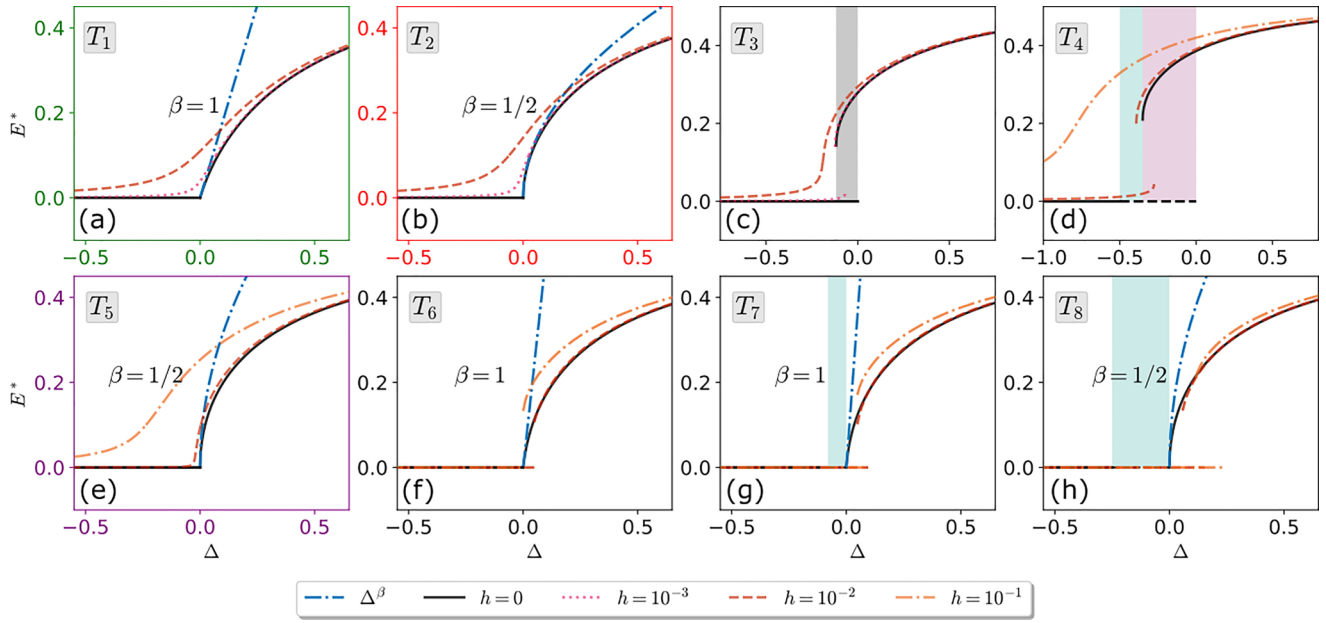


FIG. 4. Order parameter as a function of the control parameter, $\Delta = w_{EE} - w_{EE}^*$, across the eight possible types of transitions as represented in Fig. 3. In all plots revealing continuous transitions, the dot-dashed blue curves correspond to asymptotic behavior $E^*(\Delta; h=0) \sim \Delta^\beta$, with the corresponding values of the β exponent. The shaded gray areas correspond to bistability between active and standard quiescent phases and the pink shaded area between active and excitable quiescent phases. The green shaded areas represent the excitable quiescent phase (same colors as Fig. 3). (a) At T_1 ($w_{IE} = 3$), the system exhibits a second-order transition from the standard quiescent to the active phase, consistently with the directed-percolation (DP) universality class ($E^* \sim \Delta^1$ for $\Delta \geq 0$). (b) T_2 ($w_{IE} = 3$) is also a continuous phase transition occurring through a tricritical point and is consistent with the tricritical directed percolation (TDP) universality class ($E^* \sim \Delta^{1/2}$). (c, d) In contrast, T_3 and T_4 are first-order or discontinuous phase transitions with coexistence between an active phase and one of two possible kinds of quiescence ($w_{IE} = 3$): first, a standard quiescent state (gray shaded area) and, second, an excitable quiescent state (pink shaded areas). (e) Case B ($w_{IE} = 1$) allows for a special tricritical transition (T_5) occurring through a Hopf-tricritical point ($E^* \sim \Delta^{1/2}$). (f–h) In case C ($w_{IE} = 0.8$), both T_6 and T_7 are continuous phase transitions when $h = 0$, with $E^* \sim \Delta^1$ and T_8 , $E^* \sim \Delta^{1/2}$, respectively. However, once a nonvanishing external field $h \neq 0$ is introduced (dash-dotted and dashed lines), there is bistability driven by the external field [for more details see gray shaded areas in Figs. 5(f)–5(h)]. Parameter values are set as in Fig. 3.

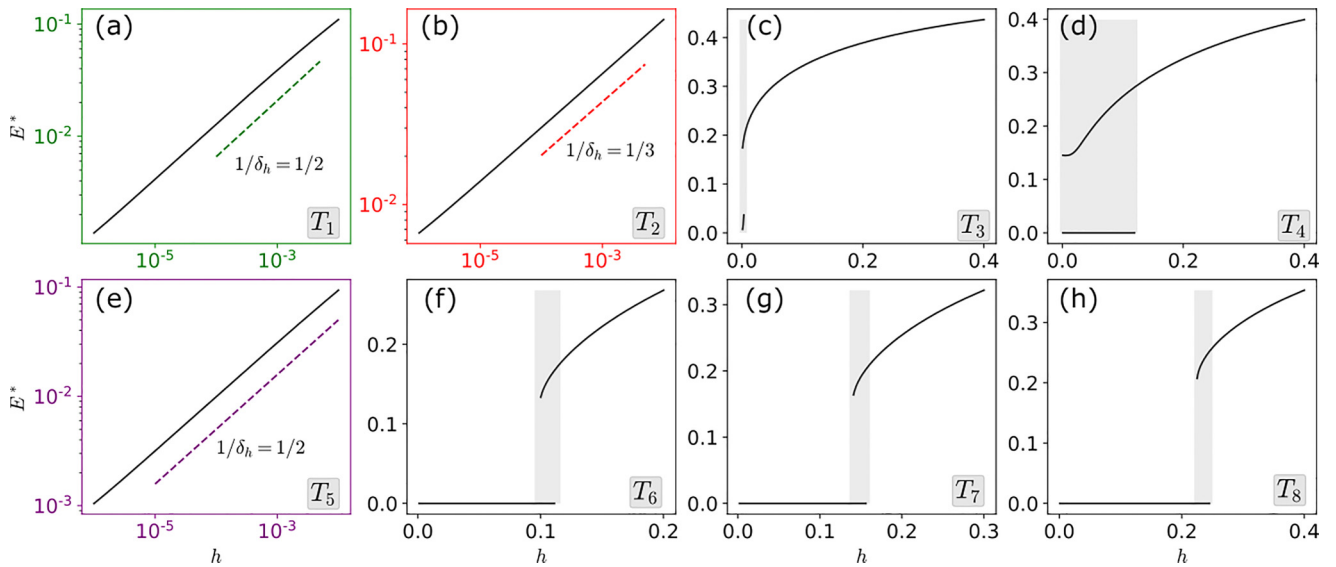


FIG. 5. Order parameter as a function of the external field right at the transition ($\Delta = 0$). Observe that three out of the eight types of transitions described here exhibit power-law scaling with the external field, i.e., $E^*(h; \Delta = 0) \sim h^{1/\delta_h}$. (a) For T_1 , $\delta_h = 2$, consistently with the DP universality class. (b) For T_2 , $\delta_h = 3$, consistently with TDP. (c, d) For T_3 and T_4 , the order parameter's response to an external field shows bistability (shaded area). (e) Transition T_5 (H +TDP), differently from the usual tricritical transition (TDP), scales with $\delta_h = 2$. (f)–(h) Remarkably, for T_6 , T_7 , and T_8 , contrary to the behavior with $h = 0$, the order parameter becomes bistable (shaded area) as the external field increases. Parameter values as in Fig. 3.

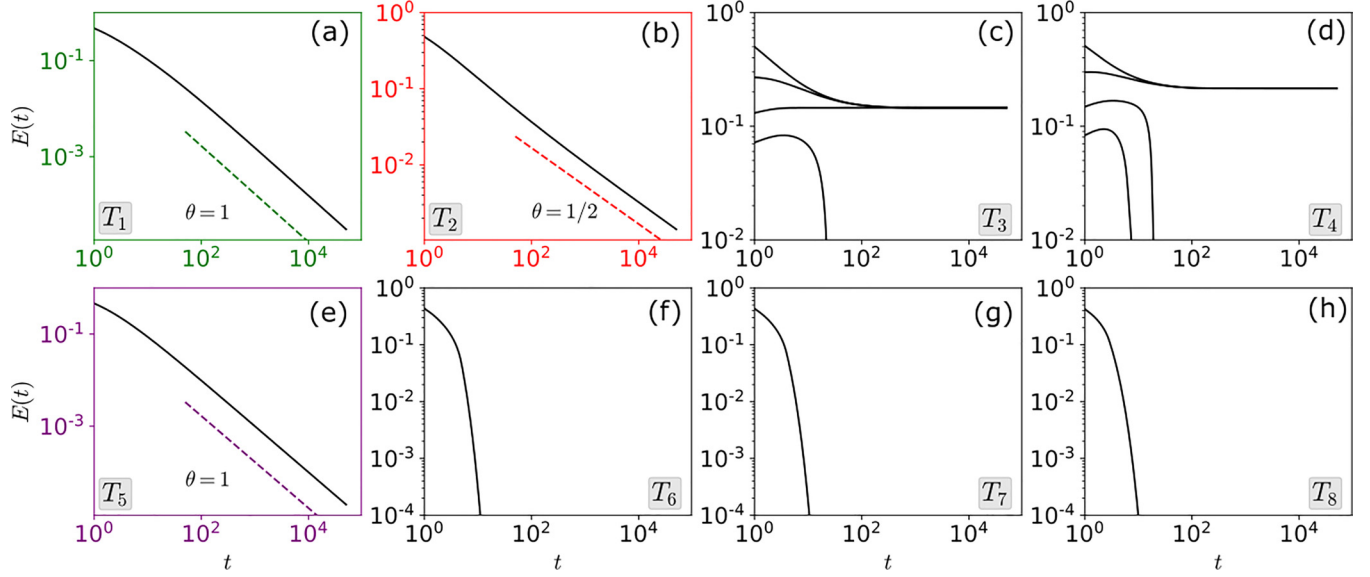


FIG. 6. Order parameter time series for the eight types of transitions. Observe that only three of them exhibit dynamical scaling $E(t) \propto t^{-\theta}$. (a) T_1 exhibits an asymptotic power-law decay with the expected DP value $\theta = 1$. (b) T_2 shows a slower asymptotic time decay in the TDP class, $\theta = 1/2$. (c) For T_3 , the saddle-node bifurcation gives rise to bistability between an active and a quiescent phase. (d) T_4 behaves very similarly to T_3 but frustrated oscillations drive the system more easily to regions II and III, so the bistability is between active and excitable quiescent phases. (e) T_5 is a genuine second-order phase transition with $\theta = 1$. (f)–(h) T_6 , T_7 , and T_8 are not genuine continuous transitions and show no signatures of dynamic scaling, but rather an exponential decay to quiescence. Parameter sets as in Fig. 3.

$\tau_t = 2$, and $\gamma = 2$ [see the distributions of sizes S , durations T , and average sizes as a function of durations in Figs. 9(a), 9(d), and 9(g), respectively]. Moreover, the averaged avalanche shape is approximately an inverted parabola throughout the T_1 line [Figs. 10(a) and 10(b)], collapsing for different durations with $\gamma = 2$, even if with some asymmetry (see Sec. V for a more in-depth discussion on avalanche shapes).

Thus, in summary, at the line of transcritical bifurcations (T_1) separating a standard quiescent from the active phase, the Wilson-Cowan stochastic model exhibits a genuine critical point in the DP class, a result that is consistent with recent analyses of de Candia *et al.* [33] for their specific choice of parameter values.

TABLE I. Summary of mean-field exponents for the discussed continuous phase transitions [13,55].

	DP	TDP	H+TDP
Codim.	1	2	3
β	1	1/2	1/2
δ_h	2	3	2
θ	1	1/2	1
δ	1	1	1
η	0	0	2
ν_{\parallel}	1	1	1
τ	3/2	3/2	5/4
τ_t	2	2	2
γ	2	2	4

B. T_2 : Tricritical directed percolation (saddle-node-transcritical bifurcation)

The tricritical point in case A [see Fig. 3(a)] corresponds to a saddle-node transcritical (SNT) bifurcation—i.e., where the lines of transcritical and saddle-node bifurcations intersect without further degeneracies [62,63]. Thus, in order to tune to this transition point one needs to set two parameters in the phase diagram (w_{EE} , w_{EI}), as explicitly calculated in Appendix B. An analysis in terms of the fields Σ and Λ (analogously to the previous case) shows that there is only one vanishing eigenvalue at the transition, and, thus, the second field is irrelevant for scaling. Therefore, T_2 is expected to be described by the mean-field tricritical directed percolation universality class (TDP) [13]. Indeed, considering the leading-order terms in a power expansion in both Δ and h , one has

$$E^*(\Delta, h = 0) \approx \sqrt{\frac{\Delta}{w_{IE}}} + O(\Delta), \quad (25)$$

$$E^*(h, \Delta = 0) \approx \left[\frac{3[w_{IE}^2 - (\alpha + w_{II})^2]h}{w_{IE}^2[(\alpha^2 - 3)w_{IE} - (\alpha^2 + 3)\alpha]} \right]^{\frac{1}{3}} + O(h^{\frac{1}{2}}), \quad (26)$$

from where $\beta = 1/2$ [Fig. 4(b)] and $\delta_h = 3$ [Fig. 5(b)], as expected for the TDP universality class.

At the transition, the lowest order correction of Eq. (22) in Σ is $O(\Sigma^3)$, so that asymptotically $\Sigma \propto t^{-1/2}$ and, hence, $\theta = 1/2$, as numerically confirmed in Fig. 6(b). Once again, considering the linear relationship between $E(t)$ and $I(t)$, both densities share this scaling.

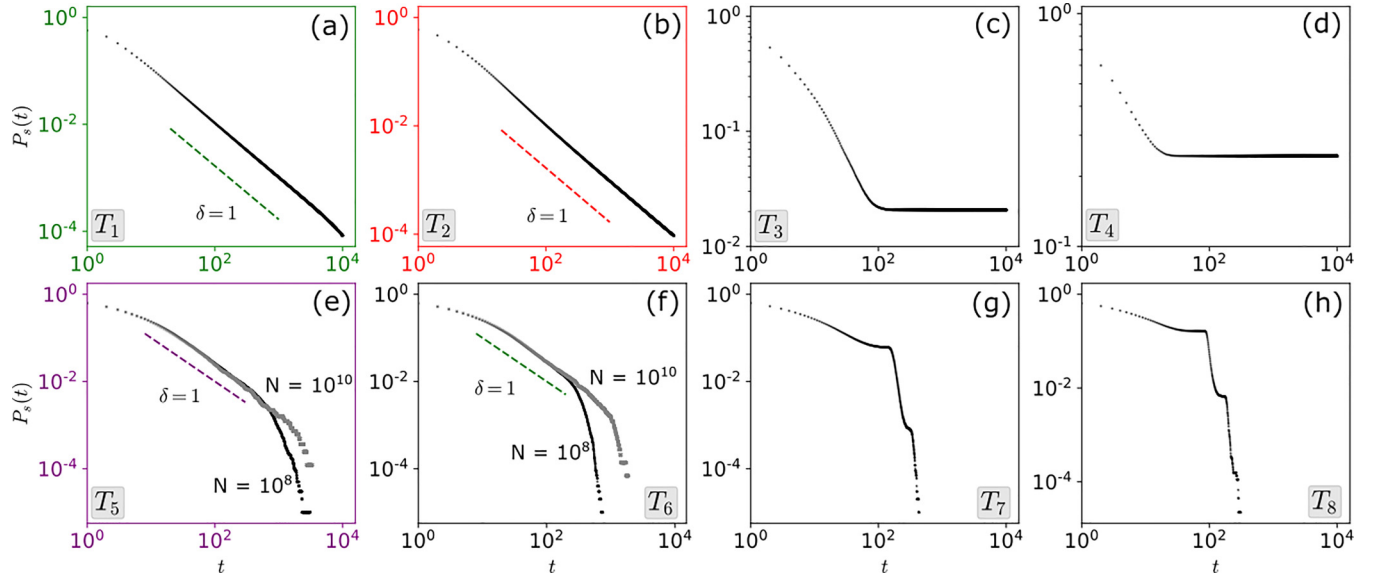


FIG. 7. Survival probability as a function of time. The survival probability at second-order phase transitions scales as $P_s(t) \propto t^{-\delta}$. Black dots stand for the numerical simulations (for the same parameters as Fig. 3 and $N = 10^8$) and dashed lines show the corresponding exponent value. (a) T_1 belongs to the DP universality class, i.e., $\delta = 1$. (b) T_2 belongs to TDP so that $\delta = 1$ (the same as DP). (c), (d) For the first-order phase transitions, the system's survival probability converges to a nonvanishing value as $t \rightarrow \infty$ due to the possibility of being attracted to the active phase. (e) For T_5 , $\delta = 1$ as in the previous continuous transitions, but with stronger finite-size effects. (f) For T_6 , the system shows a behavior similar to T_5 : a decay with $\delta = 1$ and strong finite-size effects. (g), (h) The survival probability shows a peculiar behavior of several sharp decays with some small plateaus, which stem from the excitability of the quiescent phase.

Finally, the exponent for the survival probability remains $\delta = 1$ [see Fig. 7(b)], $\eta = 0$ [see Fig. 8(a)], $\tau = 3/2$ [Fig. 9(b)], $\tau_t = 2$ [Fig. 9(e)], and $\gamma = 2$ [Fig. 9(h)], all of which are consistent with the expected values in the TDP class (see Table I).

C. T_3 : Standard discontinuous transition (saddle-node bifurcation)

The line of saddle-node bifurcations [see Fig. 3; Eq. (11)] defines the third type of transition, T_3 , to go from a standard quiescent state to the active phase. This type of transition is

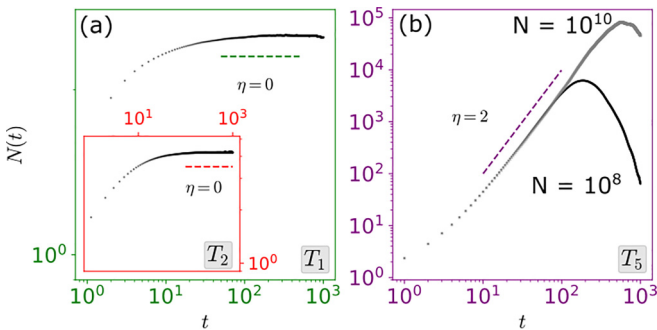


FIG. 8. Mean number of particles $N(t)$ in spreading experiments in *bona fide* continuous phase transitions (i.e., T_1 , T_2 , and T_5), at which one expects $N(t) \sim t^\eta$. Simulations with the same parameters as Fig. 3 with $N = 10^8$ (a) and $N = 10^8$ and $N = 10^{10}$ (b). (a) For T_1 and T_2 , we obtain results compatible with $\eta = 0$, as expected for DP and TDP as well as, in general, for mean-field theories. (b) On the other hand, for T_5 we obtain the unusual result $\eta = 2$, with strong finite-size effects.

characterized by a discontinuous jump in the order parameter and includes an intermediate regime of bistability, where both the active and the standard quiescent state are stable [see Figs. 3(a) and 4(c)]. The regime of coexistence lasts until, at a second bifurcation, the quiescent phase loses its local stability. Given that the transition is discontinuous, the exponents β and δ_h are not properly defined [Fig. 5(c)]. Similarly, neither the activity nor the survival probability decay to 0 for initial conditions in the basin of attraction of the active phase [see Figs. 6(c) and 7(c)], so that the exponents θ and δ are not well defined either.

Thus, in summary, the T_3 transition is a standard first-order or discontinuous transition into a quiescent or absorbing state [5,13].

D. T_4 : Discontinuous transition from an excitable quiescent state (saddle-node bifurcation)

A scenario very similar to T_3 occurs at T_4 , which appears in all three possible phase diagrams (A, B, and C; see Fig. 3). Transition T_4 is also discontinuous with phase coexistence, but it differs from T_3 in the fact that—as illustrated in Fig. 4(d)—the quiescent phase that coexists with the active one in the regime of bistability is of the excitable type, rather than the standard one. The bistability regime ends where the excitable quiescent phase loses its global stability in favor of the active one, at a discontinuity-induced transition (black-dashed line in Fig. 3). For the same reasons as in T_3 , none of the critical exponents is well defined [see Figs. 5(d), 6(d), and 7(d)].

Thus, in summary, T_4 is a discontinuous transition with bistability, but with the peculiarity of having an excitable quiescent state coexisting with the active one.

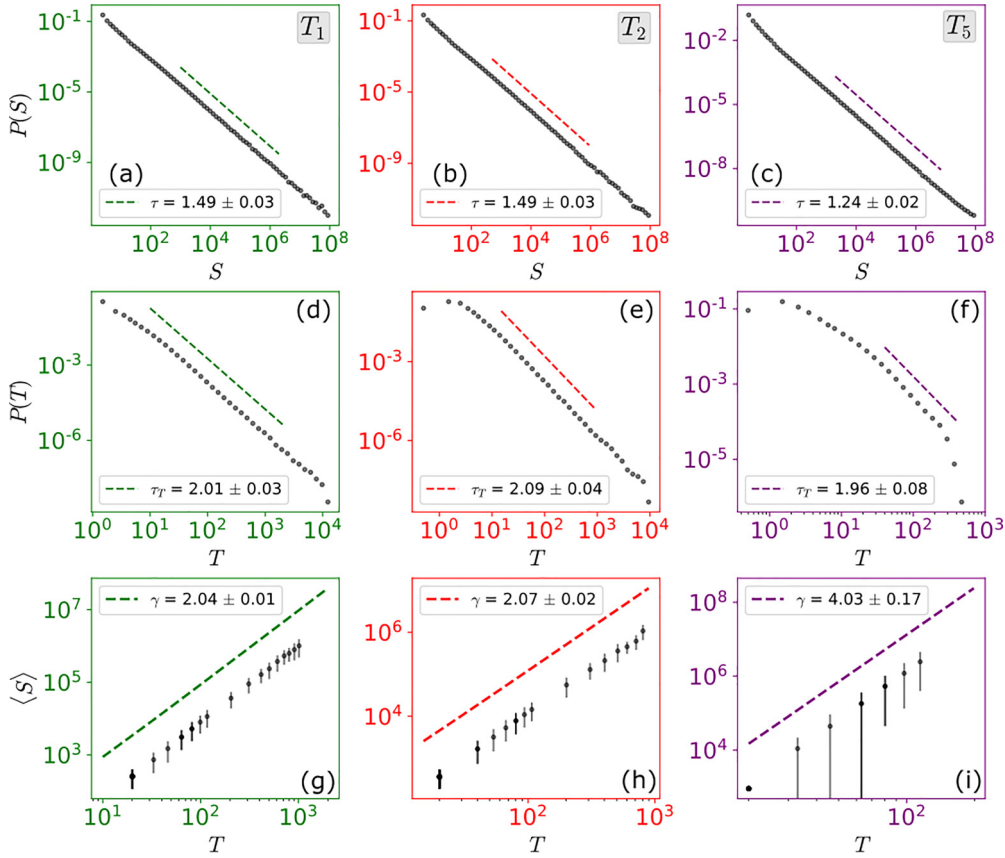


FIG. 9. Avalanche analysis. Simulations using Gillespie’s algorithm for the same parameters as in Fig. 3 and network size $N = 10^8$. In this case, we report results only for true (or *bona fide*) continuous phase transitions, for which scale-free avalanches emerge, i.e., T_1 , T_2 , and T_5 . For the T_1 transition, one obtains results as expected for DP: (a) $\tau \approx 3/2$, (d) $\tau_t \approx 2$, and (g) $\gamma \approx 2$. For T_2 , the system behaves consistently with TDP: (b) $\tau \approx 3/2$, (e) $\tau_t \approx 2$, and (h) $\gamma \approx 2$, i.e., TDP and DP share the same avalanche exponents. Finally, for the T_5 transition, (c) $\tau \approx 5/4$, (f) $\tau_t \approx 2$, and (i) $\gamma \approx 4$. The exponents τ and τ_t were obtained with the Maximum Likelihood Estimator (MLE) method [69].

E. T_5 : Hopf tricritical directed percolation (Hopf saddle-node-transcritical bifurcation)

As illustrated in Fig. 3(b), Case B exhibits a *codimension 3* bifurcation point at which the tricritical point (codimension 2) and the line of Hopf bifurcations meet. This transition occurs only in case B, for the particular choice of parameters for which the vertical line of Hopf bifurcations ends up exactly at the tricritical point, $w_{IE}^* = \alpha + w_{II}$, as derived from Eq. (12) and Eq (B3) in Appendix B. Using this constraint, one can easily find that the location of the T_5 point is specified by the following set of conditions (see Appendix B): $w_{EE} = 2\alpha + w_{II}$ and $w_{EI} = w_{IE}$.

Let us first write the stationary solutions of the dynamical equations (3) and (4) up to leading order in Δ at vanishing h and, also, up to leading order in h at vanishing Δ ,

$$E^*(\Delta; h = 0) \approx \sqrt{\frac{\Delta}{\alpha + w_{II}}} + O(\Delta), \quad (27)$$

$$E^*(h; \Delta = 0) \approx \sqrt{\frac{h}{3(\alpha + w_{II})^2}} + O(h). \quad (28)$$

These imply $\beta = 1/2$ [as illustrated in Fig. 4(e)] and $\delta_h = 2$ [see Fig. 5(e)]. Note that β coincides with its counterpart for TDP (as expected for a tricritical-like point) but, curiously

enough, δ_h does not; it instead coincides with its value in the DP class. Therefore, the static exponents at T_5 do not fully comply with either of the well-known universality classes.

To make further progress, it is convenient to introduce, as before, the equations for $\Sigma(t)$ and $\Lambda(t)$, as defined in Eq. (22) and Eq. (23):

$$2\dot{\Sigma}(t) = \Delta(\Sigma + \Lambda) + 4(w_{II} + \alpha)\Lambda - \frac{2\alpha}{w_{II} + \alpha}\Sigma^2 - 4\Sigma\Lambda - \frac{2\alpha}{w_{II} + \alpha}\Lambda^2 + O, \quad (29)$$

$$2\dot{\Lambda}(t) = \Delta(\Sigma + \Lambda) - 4\Lambda^2 - \frac{4\alpha}{w_{II} + \alpha}\Sigma\Lambda + O, \quad (30)$$

where $O \equiv O(\Sigma^3, \Sigma^2\Lambda, \Sigma\Lambda^2, \Lambda^3, \Delta\Sigma^2, \dots)$ stands for higher-order terms and time dependences have been omitted for simplicity. Moreover, right at the transition point ($\Delta = 0$), the dynamics simplifies to

$$\dot{\Sigma}(t) = 2(w_{II} + \alpha)\Lambda - \frac{\alpha}{(w_{II} + \alpha)}\Sigma^2 + O, \quad (31)$$

$$\dot{\Lambda}(t) = -2\Lambda^2 - \frac{2\alpha}{w_{II} + \alpha}\Lambda\Sigma + O, \quad (32)$$

where the consistency of the truncation of higher-order terms will be justified *a posteriori*.

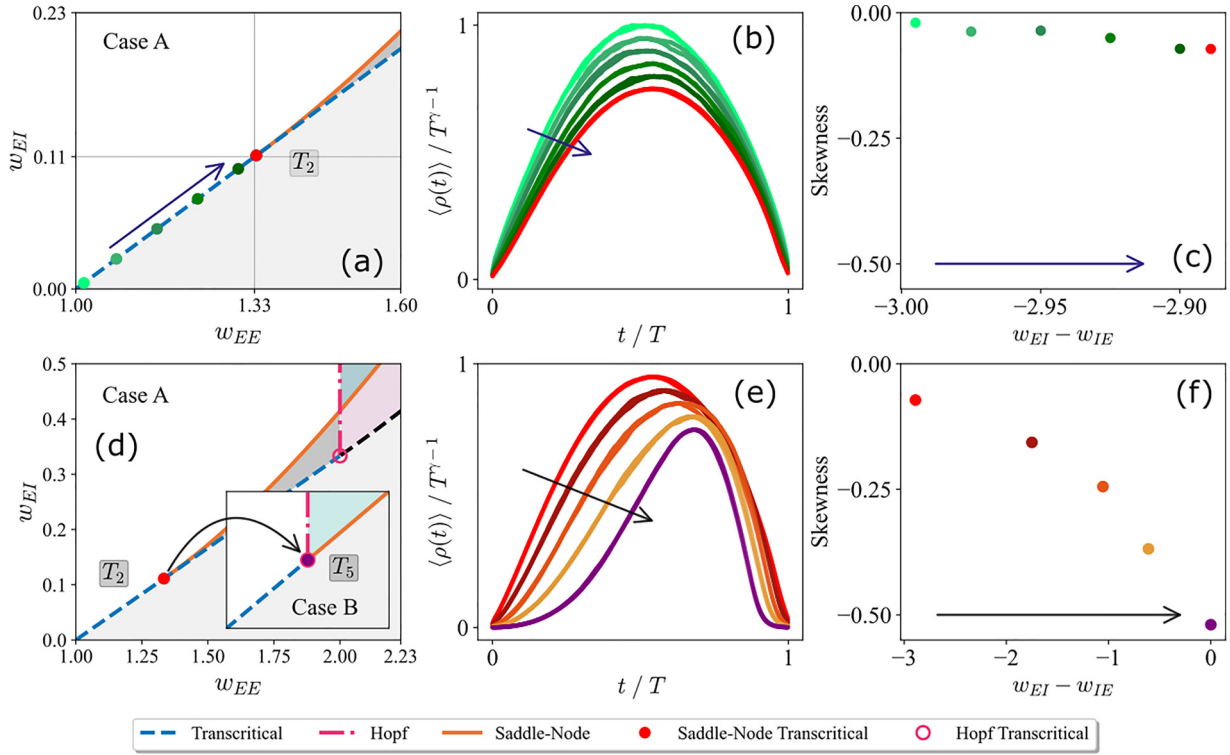


FIG. 10. Skewness and mean temporal profile of avalanches. Enlargements of Fig. 3 illustrate the excursion in parameter space (a) along a transcritical line to a tricritical point and (d) along a tricritical line to a Hopf-tricritical point (by decreasing the parameter w_{IE} , the phase diagram goes from case A to case B, which is illustrated in the inset). Panels (b) and (e) show the corresponding rescaled mean temporal profiles (avalanche shape collapses). (c) The skewness of the previous curves (b) slightly decreases as the tricritical point is approached (i.e., as the difference $w_{EI} - w_{IE}$ increases). (e) As the system approaches the $H+TDP$ transition, the curves of the mean temporal profile become progressively less symmetrical, as assessed by the skewness of the curves (f). Simulations with the same parameters as Fig. 3 and $N = 10^8$.

In particular, observe that the stability matrix around the origin becomes

$$A \propto \begin{pmatrix} 0 & w_{II} + \alpha \\ 0 & 0 \end{pmatrix} \quad (33)$$

so that the null eigenvalue is degenerate and, thus, an anomalous type of scaling is to be expected. Indeed, the previous matrix is characteristic of the normal form of a Bogdanov-Takens bifurcation [51], which has been already discussed in the context of Wilson-Cowan models [36,40] and, more in general, in the analysis of nonnormal or *nonreciprocal phase transitions* [64].

It is important to observe that the only linear term in the first equation, Eq. (31), $2(w_{II} + \alpha)\Lambda(t)$, has a positive coefficient. This implies that at criticality $\Lambda(t)$ needs to decay to zero faster than $\Sigma(t)$ as otherwise the overall right-hand side would be positive asymptotically in time (which cannot possibly happen at criticality). Therefore, given that $\Sigma(t)$ needs to decay slower than Λ , the slowest-decaying nonlinear term in Eq. (31) is the one proportional to $-\Sigma^2$. Knowing that asymptotically, $\dot{\Sigma} \propto -b\Sigma^2$, with $b = \alpha/(w_{II} + \alpha)$ one readily finds that $\Sigma \sim t^{-1}/b$ and, therefore, $\theta = 1$ [as numerically verified; see Fig. 6(e)]. Finally, plugging this result into the second equation, Eq. (32), comparing constants and exponents, one readily finds that $\Lambda \sim t^{-2}$. Observe that, indeed, as anticipated, $\Lambda(t)$ decays faster than $\Sigma(t)$: $\Lambda \sim \Sigma^2$, which justifies the truncation of higher-order terms in the previous equations.

Using these observations one concludes that, right at the transition point $\Delta = 0$, the dynamical scaling is consistent with DP because, since Λ decays faster, it does not influence the decay of Σ (dominated by a quadratic term). This result is surprising as we are dealing with a tricritical point so, *a priori*, one would expect TDP-like scaling.

The situation is different away from the critical point ($\Delta > 0$). In this case, it is convenient to focus on the equation for Λ , Eq. (30). At stationarity, the linear positive term (proportional to Δ) needs to cancel with the leading nonlinear one. *A priori*, the linear positive term is either the one proportional to $\Delta\Sigma$ or the one proportional to $\Delta\Lambda$, depending on the scaling dimensions of Σ and Λ . Note that both yield that Λ scales as $\Lambda \propto \Delta$. Now, focusing on the first equation [Eq. (29)], the leading positive term is $4(w_{II} + \alpha)\Lambda$ (which scales as Δ , while $\Delta(\Sigma + \Lambda)$ is a higher-order contribution). This leading term needs to be comparable with the leading negative term, which is the one proportional to $-\Sigma^2$ (note that the other possibility, $-4\Sigma\Lambda$, leads to a fixed value of Σ that does not change or scale with Δ and, therefore, it is not a solution). The resulting scaling renders $\Lambda \sim \Sigma^2$, which is consistent with the temporal scaling. And, then, one derives $\Sigma \sim \Lambda^{1/2} \sim \Delta^{1/2}$, i.e., $\beta = 1/2$ (while the field Λ scales with an exponent $\beta_\Lambda = 1$).

Therefore, since (1) the order-parameter exponent is that of the TDP class, $\beta = 1/2$, (2) the time-decay exponent $\theta = 1$ differs from its TDP value, and (3) $\nu_{||} = 1$ (as it is the case for

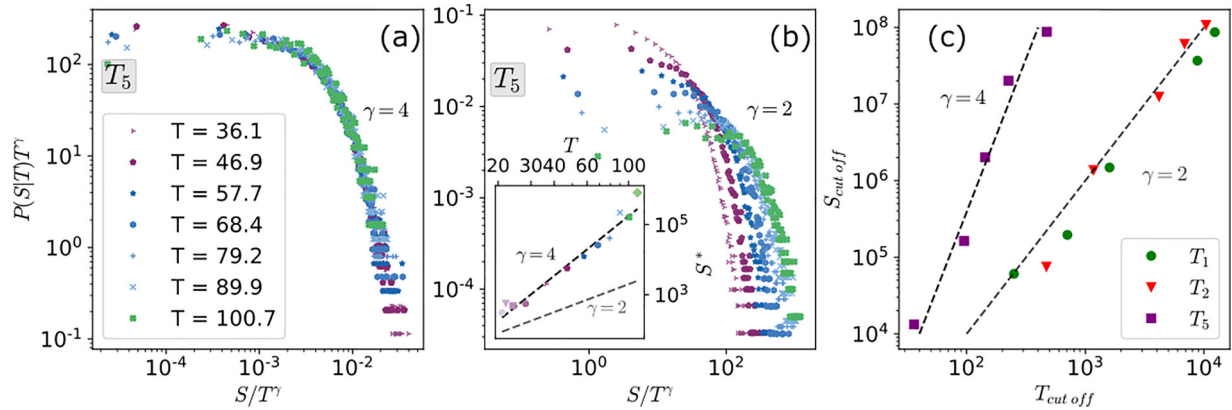


FIG. 11. Conditional probability of avalanche sizes given durations, $P(S|T)$, in *bona fide* continuous phase transitions (i.e., T_1 , T_2 , and T_3). Numerical results obtained with Gillespie’s algorithm for the same parameters as Fig. 3; for (a) and (b), the system is poised at T_3 with a network size of $N = 10^8$; for (c) each transition is simulated for sizes $N = 10^4, 10^5, 10^6, 10^7$, and 10^8 . (a) $P(S|T)$ collapses into a single curve when one sets $\gamma = 4$. (b) In contrast, for $\gamma = 2$ there is no curve collapse. Furthermore, in the inset, one observes that the peaks of $P(S|T)$ (S^*) scale with $S^* \sim T^\gamma$, with $\gamma = 4$. (c) Cutoff for size and duration distributions; one scales as a power of the other with the corresponding value of the exponent γ [67,68].

all mean-field transitions), then it follows that

$$\theta \neq \beta/\nu_{\parallel}, \quad (34)$$

which violates one of the basic scaling relations in systems with quiescent states, i.e., Eq. (17).

Let us remark that a similar violation of scaling was found by Noh and Park [65] in a model with quiescent states and two relevant fields: an “excitatory” and a “repressing” one. In both cases—here and [65]—the breakdown of scaling stems from the nontrivial interplay between these two fields with opposing effects.

Similarly to the other transitions, the survival probability decays with an exponent $\delta = 1$, albeit with a higher sensitivity to system size [see Fig. 7(e)]. Also, consistently with the scaling relation $\tau_t = \delta + 1$ [55], the avalanche distribution of durations scales with the same exponent as in DP and TDP, $\tau_t \approx 2$ [Fig. 9(f)].

In contrast with the rest of the second-order phase transitions [see Fig. 8(a)], the growth of the total activity in spreading experiments right at criticality is $N(t) \sim t^2$, yielding $\eta = 2$ [Fig. 8(b)]. This observation is rather surprising for a mean-field model as most mean-field universality classes are characterized by $\eta = 0$ (i.e., absence of an “anomalous dimension” [3,8]).

In order to shed some light on this result, let us observe that the linearized dynamics at criticality—controlled by the normal form of a Bogdanov-Takens bifurcation [Eq. (33)]—is such that a small initial perturbation can be largely amplified before decaying back to quiescence, i.e., around the fixed point the system is excitable. In particular, if the perturbation consists of a single seed (as in spreading experiments), the number of active sites in surviving runs grows in a deterministic way until a maximum size is reached, and, then, the asymptotic decay toward the quiescent state (controlled by the exponent θ) begins. This initial deterministic growth—which does not occur in the DP nor TDP classes—is expected to be responsible for the anomalous value of η .

More specifically, observe that, in Eq. (31) and Eq. (32), the density Σ at first grows linearly as $\dot{\Sigma} \propto \Lambda$ and Λ can

be approximately taken as a constant because its negative eigenvalue vanishes. Furthermore, the total number of active sites $N(t)$ is equal to the density times an additional “volume factor,” which, owing to the deterministic expansion, grows linearly in time. Therefore, one concludes that $N(t) \sim \Sigma(t)t \sim t^2$, which yields $\eta = 2$.

Given this anomalous value and using the general scaling relations described before, one can infer other exponent values. In particular, Eq. (14) predicts $\tau = 5/4$ and Eq. (16) leads to $\gamma = 4$, which are both unusual or anomalous exponents in mean-field theories. We numerically verified both of these results; scaling compatible with $\tau \approx 5/4$ can be observed in Fig. 9(c), and with $\gamma \approx 4$ in Fig. 9(i). This latter value also gives an excellent data collapse for $P(S|T)$ [Figs. 11(a) and 11(b)] and is consistent with the scaling relation between size and duration cutoffs [Fig. 11(c)] [66–68].

In summary, the T_3 transition defines a thus far unknown universality class, which we named Hopf tricritical directed percolation ($H+TDP$). In its mean-field variant, it has a set of exponents that do not match either DP or TDP universality classes (Table I), violates at least one scaling relation, includes some anomalous exponent values, and produces highly asymmetrical avalanche shapes, as we shall show in a separate section.

A more systematic and rigorous derivation of these results, together with a field-theoretic discussion of this universality class will be presented elsewhere.

F. T_6 : Hopf-transcritical bifurcation

This type of continuous transition [see Fig. 4(f)] occurs when the line of Hopf bifurcations collides with the transcritical line [see Fig. 3(c)] and appears only in case C. This transition is peculiar in that at the critical point— independently of the initial conditions—the trajectories are attracted to region II [and, possibly, III; see Fig. 1(b)]. This occurs because the Hopf bifurcation overrides the transcritical bifurcation, and the elicited frustrated oscillations drive the system toward the switching manifold and, thus, into region II.

Once in region II, the excitatory density decays exponentially fast, dragging down the system without signatures of scaling; e.g., the time-decay exponent θ is not defined for T_6 [see Fig. 6(f)].

At the transition point [as specified by Eq. (12) and Eq. (13)], one can rewrite Eq. (18) and Eq. (19) as

$$E^*(\Delta; h = 0) \approx \frac{\alpha + w_{II}}{(\alpha + w_{II} - w_{IE})} \Delta + O(\Delta^2), \quad (35)$$

$$E^*(h; \Delta = 0) \approx \sqrt{\frac{[(w_{II} + \alpha)^2 - \alpha w_{IE}]h}{\alpha w_{IE}[w_{IE} - w_{II} - \alpha]}} + O(h). \quad (36)$$

On the one hand, Eq. (35) holds because, for $h = 0$, there is a stable equilibrium in region I for $\Delta \geq 0$, which attracts the trajectories, preventing them from falling into region II. Observe that in case C, $w_{IE} < w_{II} + \alpha$ —as the condition at the interface between case A and case C is $w_{IE} = w_{II} + \alpha$ —and, therefore, while Eq. (35) is valid and yields $\beta = 1$, Eq. (36) is misleading since the denominator is negative inside the square root so that it does not correspond to a real solution. The reason is that the previous equations are based on the naive linearization of the dynamical equations, assuming the nonvanishing part of the response function Φ . However, this assumption is invalid in the present case. Thus, for Eq. (36) and $\Delta = 0$, since trajectories fall into region II and E decays to zero exponentially fast, the absorbing state remains globally stable even as h increases from zero. Therefore, the exponent δ_h is not well defined for T_6 . Nevertheless, further increasing the external field h eventually leads to a saddle-node bifurcation and a discontinuity in the order parameter [Fig. 5(f)].

Regarding spreading exponents, we have verified that the system's survival probability decays in time with $\delta = 1$ [Fig. 7(f)] as in all other transitions—even if, similarly to T_5 , with strong finite-size effects. Also, for the same reasons as T_5 , the growth of active sizes follows $\eta = 2$ in this case.

In conclusion, T_6 exhibits a mixture of signatures of both continuous and discontinuous transitions and, thus, does not belong to any standard type of quiescent-active universality class.

G. T_7 and T_8 : Continuous transitions from quiescent-excitable to active states

The transitions represented by T_7 and T_8 happen between the quiescent excitable state and the active state [only in case C, as illustrated in Fig. 3(c)]. The first occurs through a discontinuity-induced transition (black dashed lines in Fig. 3) and the second through a tricritical point, so that they are the counterparts of T_1 and T_2 , respectively, for excitable—rather than standard—quiescent states.

Let us recall that, as explained above, a naive linearization of the quiescent excitable state (assuming $\Phi > 0$) yields eigenvalues with a nonvanishing imaginary part; in any case, the quiescent state remains stable due to frustrated oscillations that draw the system into the regions II and, possibly, III [Fig. 1(b)].

Observe that Eq.(18) and Eq. (25) remain unchanged for T_7 and T_8 , respectively. Therefore, the order parameter changes continuously with the control parameter with $\beta = 1$ and $\beta = 1/2$, respectively [Figs. 4(g) and 4(h)]. However, similarly

to transition T_6 , the denominators of Eq. (19) and Eq. (26), governing the response to an external field h at the transition point, are negative and the system asymptotically reaches region II, i.e., converges quickly to quiescence. Thus, the response to an external field coincides with that of T_6 , and the exponent δ_h is not well defined for either T_7 or T_8 as there is a discontinuous jump in the order parameter [see Figs. 4(g) and 4(h) as well as Figs. 5(g) and 5(h)].

On the one hand, also as in T_6 , the asymptotic dynamics of the order parameter in the T_7 and T_8 transitions exhibit an exponential time decay [Figs. 6(g) and 6(h)]. On the other hand, the overall behavior of the survival probability, for T_7 and T_8 , shows an intermediate plateau, as opposed to the smooth decay to zero observed for T_6 [Figs. 7(f)–7(h)]. These plateaus stem from the fact that the excitable quiescent phase is well established before the transitions take place (in opposition to what happens in T_6).

Thus, in summary, the T_7 and T_8 transitions also exhibit a mixture of features of continuous and discontinuous phase transitions.

V. THE AVERAGE SHAPE OF AVALANCHES

The scaling of the mean avalanche shape (also called “mean temporal profile”)—i.e., the fact that the averaged shape of avalanches with different sizes and durations can be collapsed into a single curve by using the adequate value of critical exponents—has been used as a signature of criticality in nonequilibrium systems with absorbing states [70]. As already mentioned, the DP and TDP universality classes are known to typically have symmetric inverted parabolic mean-temporal profiles of avalanches, a consequence of time-reversal symmetry [71]. The asymmetry in the mean temporal profile, when found, reflects a break in such a symmetry [36,72].

In the present Wilson-Cowan model, we observed that, when the transition to quiescence occurs in the neighborhood of T_5 (or $H+TDP$) point in parameter space, avalanche shapes exhibit a nontrivial behavior. In particular, as illustrated in Fig. 10(a), when one follows the DP (T_1) line towards the TDP (T_2) point in case A, the mean temporal profile of avalanches acquires only a slight asymmetry [Fig. 10(b)] as quantified by the increase in the absolute value of its skewness [Fig. 10(c)]. This observation agrees with recent results that show that the introduction of an inhibitory population causes a small tilt on the mean temporal profile at the DP transition [33,34,36].

However, remarkably, studying the system at the TDP transition as the overall parameters transition from case A to case B [Fig. 10(d)], the avalanche mean temporal profile becomes progressively more and more asymmetric, with its skewness reaching a maximal absolute value—i.e., maximal asymmetry as illustrated in Fig. 10(f)—at the $H+TDP$ transition [Fig. 10(e)]. This type of asymmetric or skewed avalanche shape has also been found in other studies. However, the sign of the skewness, i.e., whether the shapes are left- or right-skewed, does not seem to be a universal feature as it may depend on model details and parameter values [36]. A more general and systematic study of such asymmetries is left for future work.

VI. CONCLUSIONS

By means of detailed scaling analyses as well as extensive numerical simulations, we have thoroughly analyzed all possible types of phase transitions between active and quiescent phases that the stochastic Wilson-Cowan model exhibits.

On the one hand, under some conditions, the model exhibits the standard phenomenology of systems with quiescent or absorbing states, i.e., two phases (active and quiescent) as well as a phase transition separating them. This transition can be a continuous one (in the mean-field directed-percolation class), a discontinuous one with hysteresis, or a tricritical transition in the tricritical-directed-percolation class, at the point where the previous two types of transitions meet [4,5,13].

On the other hand, a key feature of the mean-field Wilson-Cowan model is that—in addition to the standard active and quiescent phases—there is another “excitable quiescent” phase. In particular, the phase diagram describing the model at a mean-field level exhibits a line of Hopf bifurcations to the left of which there is a standard quiescent state, while, to the right of it, the convergence towards the quiescent state occurs in an oscillatory way (involving complex eigenvalues). Such pseudo-oscillations are nevertheless “frustrated” as the system enters inhibition-dominated regions of the state space (region II or region III in Fig. 1) and, then, activity decays exponentially fast to zero. Observe that in this regime, owing to the nonnormality of the stability matrix (see below), small perturbations to quiescence can be transiently amplified, before decaying back again to quiescence, hence the name “excitable quiescent” phase (or also, possibly “reactive” phase, see [28,36,54,73,74]).

Both of the previous features—i.e., the presence of a line of Hopf bifurcations and of an excitable-quiescent phase—stem from the existence of an inhibitory population or field and cannot possibly appear in simpler models for activity propagation, such as directed percolation or the contact process which include only one field, describing the excitatory activity. These two ingredients are at the root of the enriched set of possible phase transitions that the system can exhibit with respect to standard ones.

Our analyses reveal that the Wilson-Cowan model can exhibit three possible types of (bidimensional) phase diagrams (as illustrated in Fig. 3) that can be viewed as sections of a larger (three-dimensional) phase diagram. These three cases (A, B, and C) differ from one another in the relative position of the (vertical) line of Hopf bifurcations with respect to the tricritical point (and are controlled by a single parameter, w_{IE} in Fig. 3). Careful inspection of the three of them reveals the existence of eight different types of phase transitions, labeled T_1, T_2, \dots , and T_8 , respectively.

Three of them are usual ones separating active from standard quiescent phases and are well known from the theory of phase transitions: (1) a (mean-field) directed-percolation (DP), continuous transition (T_1); (2) a (mean-field) tricritical directed-percolation (TDP) (T_2); and (3) a (mean-field) discontinuous transition with bistability and hysteresis (T_3). These three cases correspond to transcritical, saddle-node-transcritical, and saddle-node bifurcations, respectively and exhibit the expected features for their corresponding well-known universality classes.

In particular, let us remark that our results for the DP case (T_1) are consistent with those recently reported by de Candia *et al.* [33]. These authors chose to study the case where $w_E \equiv w_{EE} = w_{IE}$ and $w_I \equiv w_{EI} = w_{II}$; for this choice of parameters, one is in the T_1 case [actually, Eq. (8) becomes $w_E - w_I = \alpha$, which is the condition for criticality in [33]]. Similarly, for T_2 our results reproduce the TDP class as first described in [13] (note that recent research has also considered the possibility of a tricritical point in neuronal models with a population of inhibitory units [36,75]). Finally, for T_3 , we observe the standard features from discontinuous phase transitions into absorbing states, such as hysteresis [13,15].

Each of the previous three transitions has a counterpart in which the quiescent phase is not a standard one but a quiescent-excitable one: the twin of T_1 is a transcritical bifurcation from the quiescent excitable state (labeled T_7), the twin of the tricritical T_2 is T_8 , and the twin of T_3 is a discontinuous transition, which exhibits bistability between the active and the quiescent-excitable states (labeled T_4). A peculiar feature of the continuous ones, i.e., T_7 and T_8 , is that their response to an external field is anomalous: even if they are continuous transitions, once the field is introduced they become discontinuous. In other words, the addition of a small external field drives slightly active states to become quiescent (a phenomenon that stems from the excitability of the quiescent state). As a consequence, critical exponents such as δ_h are not well defined, so T_7 and T_8 share features of both continuous and discontinuous phase transitions.

The remaining transitions are unusual and involve entering the active phase right at the point where a Hopf bifurcation also occurs (i.e., they correspond to higher-codimension bifurcations). In particular, T_6 describes the situation in which the Hopf bifurcation falls on top of a transcritical bifurcation, whereas T_5 occurs at the special point in which the Hopf bifurcation falls exactly on top of the tricritical (or SNT) point, which is possible only in case B.

For T_6 , the transition is adjacent to the excitable-quiescent phase, and, thus, one observes the same phenomenon as for T_7 and T_8 , when introducing an external field. Even if the transition (T_6) is continuous, the response to a small external field is anomalous, giving rise to a discontinuity and preventing the exponent δ_h to be well defined, so again, T_6 exhibits features of both continuous and discontinuous phase transitions.

Finally, T_5 is by far the most interesting and less trivial transition. We have named it Hopf-tricritical directed percolation ($H+TDP$) transition as it occurs when the Hopf line collides with the tricritical point, giving rise to a codimension 3 transition. In this case, both eigenvalues of the stability matrix vanish at the transition point, so that the matrix has the normal form of a Bogdanov-Takens bifurcation. From the point of view of power-counting and dimensionality analyses, this fact has important implications, as carefully discussed above. In particular, a key aspect is that the scaling features are controlled by different terms (1) right at criticality and (2) slightly in the active phase. This dichotomy entails a remarkable and surprising violation of some well-established scaling laws. It is noteworthy, though, that a breakdown of scaling in a somehow similar model—including also a second inhibitory-like field—has been recently reported by Noh and Park [65].

Another anomalous feature of T_5 is that the exponent controlling the growth of the total number of particles in spreading experiments, η , does not vanish, i.e., $\eta = 2$, as opposed to what happens in (mean-field) DP and most other mean-field phase transitions (as it is related with perturbative corrections to mean-field behavior [61]). Moreover, the scaling anomaly of the H +TDP transition is also reflected in its avalanche exponents: while the duration exponent $\tau_r = 2$ is consistent with DP and TDP, the size-distribution exponent $\tau = 5/4$ and crackling noise exponent $\gamma = 4$ are different from the usual ones ($\tau = 3/2$ and $\gamma = 2$, respectively).

A more systematic field-theoretical analysis of the H +TDP universality class—as well as its implementation in finite-dimensional substrates—is left for future work.

A relevant hallmark of standard models in the DP class is the symmetry in the mean temporal profile of avalanches, which reveals time-reversal invariance [71,72]. On the contrary, the mean temporal profile in T_5 shows a strong asymmetry that we have quantified in terms of negative skewness. Previous work has shown that the introduction of inhibition tilts the once symmetric inverted parabolas produced by models in the DP universality class [34,36]. We further propose that not only the strength of the inhibitory coupling slightly tilts the mean temporal profiles, but that the combination of the proximity to the excitable quiescent phase and to the onset of frustrated oscillations promotes even greater distortions. Considering the inherent difficulties in assessing avalanche exponents from experimental data, the asymmetry in the avalanche shape collapse may turn out to be a useful additional tool to more directly reveal proximity to this anomalous transition.

Last but not least, it is also worth stressing that the nature of the phase diagram and phase transitions that we have reported for the mean-field Wilson-Cowan model may change when sparse networks are considered [76]. In particular, the presence of enhanced stochastic effects, stemming from the finite connectivity of each unit, can significantly alter the dynamics and induce novel phenomena [36]. The study of the interplay between the transitions discussed here and such additional stochastic effects remains to be pursued. Similarly, the effect of structural heterogeneity, e.g. the presence of local excitation or inhibition imbalances, that could potentially lead to extended critical (Griffiths) phases [77–79], remains as an open challenge for future work.

ACKNOWLEDGMENTS

M.A.M. acknowledges the Spanish Ministry and Agencia Estatal de investigación (AEI) through Project of I+D+i Ref. PID2020-113681GB-I00, financed by MICIN/AEI/10.13039/501100011033 and FEDER “A way to make Europe,” as well as the Consejería de Conocimiento, Investigación Universidad, Junta de Andalucía, and European Regional Development Fund, Project No. P20-00173 for financial support. H.C.P. acknowledges CAPES (PrInt Grant No. 88887.581360/2020-00) and is grateful for the hospitality of the Statistical Physics group at the Instituto Interuniversitario Carlos I de Física Teórica y Computacional at the University of Granada during

her six-month stay, during which part of this work was developed. M.C. acknowledges support by CNPq (Grants No. 425329/2018-6 and No. 308703/2022-7), CAPES (Grant No. PROEX 23038.003069/2022-87), and FACEPE (Grant No. APQ-0642-1.05/18). This article was produced as part of the activities of Programa Institucional de Internacionalização (PrInt). We are also very thankful to R. Corral, S. di Santo, V. Buendia, J. Pretel, and I. L. D. Pinto for valuable discussions and comments on previous versions of the manuscript.

APPENDIX A: GILLESPIE’S ALGORITHM

The stochastic version of the Wilson-Cowan model [28] was simulated using Gillespie’s algorithm [80,81], following these steps:

Step 0. Initialize the system; for spreading experiments and avalanche analyses, only an excitatory site is active at $t = 0$

Step 1. At each time step, calculate the transition rates for each neuron—if active, $\Phi(s_i)$, and otherwise, α —and add these rates, $r = \sum_i r_i$

Step 2. The time step is chosen from an exponential distribution with rate r and added to the total-time counter and

Step 3. The site to be updated is chosen with probability r_i/r , where r_i is the transition rate of the neuron.

The size (duration) of an avalanche is counted as the total number of activations (total time) of a single instance of the simulation starting from just one excitatory activated site before returning to quiescence.

APPENDIX B: MATHEMATICAL CONDITIONS FOR THE BIFURCATION LINES AND POINTS

The mathematical condition for the tricritical point is derived from a standard linear-stability analysis of the stationary solution around zero. First of all, observe that Eq. (5) and Eq. (6) have positive solutions. One can express w_{EE} as a function of the fixed-point solution (E^*, I^*) as specified by Eq. (11):

$$w_{EE} = \frac{1}{E^*} \left[w_{EI} I^* + \Phi^{-1} \left(\frac{\alpha E^*}{1 - E^*} \right) \right]. \quad (\text{B1})$$

Expanding in power series around the origin one can readily verify the emergence of an active-state solution at the value of w_{EE}^T , specified in Eq. (8). For values $w_{EE} > w_{EE}^T$, the origin loses stability to a positive solution in a transcritical bifurcation. Defining the distance to the critical value of the control parameter, $\Delta = w_{EE} - w_{EE}^T$, the value of this nontrivial solution scales linearly with Δ as

$$E^* \sim I^* \sim [(\alpha + w_{II})^3 - w_{EI} w_{IE}^2]^{-1} \Delta. \quad (\text{B2})$$

Since $\Delta \geq 0$, this solution is positive for $(\alpha + w_{II})^3 - w_{EI} w_{IE}^2 > 0$.

Observe that, for $(\alpha + w_{II})^3 - w_{EI} w_{IE}^2 = 0$, Eq. (B2) diverges, marking where the saddle-node and transcritical bifurcations collide into a saddle-node transcritical (SNT) bifurcation or tricritical point [62,63]. The tricritical point is represented in Fig. 3 a black circle for all cases (i.e., T_2 , T_5 ,

and T_3). In cases A and C, this bifurcation has codimension 2 and occurs at

$$w_{EI}^{SNT} = \frac{(\alpha + w_{II})^3}{w_{IE}^2}, \quad (\text{B3})$$

$$w_{EE}^{SNT} = \alpha + \frac{(\alpha + w_{II})^2}{w_{IE}}. \quad (\text{B4})$$

The nontrivial solution emerges from the trivial solution with w_{EE} , and it scales with the distance to the critical value, Δ , as $E^* \propto I^* \propto \Delta^{1/2}$.

Finally, in Fig. 3 case B, a codimension 3 bifurcation emerges from an extra fine-tuning of the parameters when $w_{IE} = \alpha + w_{II}$. For this choice of parameters, at $w_{EI} = w_{IE}$, the saddle-node transcritical collides with the Hopf right at the tricritical point, T_5 . Combining Eq. (12) and Eq. (B3), the values of the control parameters, for this bifurcation, are

$$w_{EI} = \alpha + w_{II}, \quad (\text{B5})$$

$$w_{EE} = 2\alpha + w_{II}. \quad (\text{B6})$$

APPENDIX C: DO TRAJECTORIES CROSS OR SLIDE ONTO THE SWITCHING MANIFOLDS?

Piecewise continuous dynamics have two possible behaviors at the switching manifolds: sliding or crossing [48]. To determine the behavior of the Wilson-Cowan model system, we consider the Heaviside function (1) in Eq. (3) and Eq. (4):

$$\dot{x} = \begin{cases} f_x^+ \equiv -\alpha x + (1-x) \tanh(w_i x - w_j y), & \text{if } s \equiv w_i x - w_j y > 0 \\ f_x^- \equiv -\alpha x, & \text{if } s < 0 \end{cases}, \quad (\text{C1})$$

where f_x^+ (f_x^-) is evaluated to the right (left) of the switching manifold, $s = 0$.

Let us consider the switching manifold $s_E = 0$, where $E = (w_{EI}/w_{EE})I$ [Fig. 1(a)]. One can then write

$$\vec{\nabla}_{s_E} = \begin{pmatrix} \frac{\partial}{\partial E} s_E \\ \frac{\partial}{\partial I} s_E \end{pmatrix} = \begin{pmatrix} w_{EE} \\ -w_{EI} \end{pmatrix}, \quad (\text{C2})$$

$$\vec{f}^+ = \begin{pmatrix} -\alpha E + (1-E) \tanh(w_{EE}E - w_{EI}I) \\ -\alpha I + (1-I) \tanh(w_{IE}E - w_{II}I) \end{pmatrix}^T, \quad (\text{C3})$$

$$\vec{f}^- = \begin{pmatrix} -\alpha E \\ -\alpha I + (1-I) \tanh(w_{IE}E - w_{II}I) \end{pmatrix}^T. \quad (\text{C4})$$

When the system reaches the switching manifold, the trajectories will cross it or slide on it depending on the sign of $(\vec{f}^+ \cdot \vec{\nabla}_{s_E})(\vec{f}^- \cdot \vec{\nabla}_{s_E})$ at the switching manifold:

$$\begin{aligned} \vec{f}^+ \cdot \vec{\nabla}_{s_E} &= -\alpha(w_{EE}E - w_{EI}I) \\ &\quad + w_{EE}(1-E) \tanh(w_{EE}E - w_{EI}I) \\ &\quad - w_{EI}(1-I) \tanh(w_{IE}E - w_{II}I), \end{aligned} \quad (\text{C5})$$

$$\begin{aligned} \vec{f}^- \cdot \vec{\nabla}_{s_E} &= -\alpha(w_{EE}E - w_{EI}I) \\ &\quad - w_{EI}(1-I) \tanh(w_{IE}E - w_{II}I). \end{aligned} \quad (\text{C6})$$

Given that at the switching manifold, $w_{EE}E = w_{EI}I$:

$$\begin{aligned} \vec{f}^+ \cdot \vec{\nabla}_{s_E} &= -w_{EI}(1-I) \\ &\quad \times \tanh\left(\frac{w_{IE}(w_{EI} - w_{II})}{w_{EE}}I\right), \end{aligned} \quad (\text{C7})$$

$$\begin{aligned} \vec{f}^- \cdot \vec{\nabla}_{s_E} &= -w_{EI}(1-I) \\ &\quad \times \tanh\left(\frac{w_{IE}(w_{EI} - w_{II})}{w_{EE}}I\right), \end{aligned} \quad (\text{C8})$$

$$\begin{aligned} (\vec{f}^+ \cdot \vec{\nabla}_{s_E})(\vec{f}^- \cdot \vec{\nabla}_{s_E}) &= [w_{EI}(1-I) \\ &\quad \times \tanh\left(\frac{w_{IE}(w_{EI} - w_{II})}{w_{EE}}I\right)]^2. \end{aligned} \quad (\text{C9})$$

For $(\vec{f}^+ \cdot \vec{\nabla}_{s_E})(\vec{f}^- \cdot \vec{\nabla}_{s_E}) > 0$, the trajectories cross the switching manifold and cannot cross back. Observe that, when $w_{EE}/w_{EI} < w_{IE}/w_{II}$, the flow points to region II, making it a trapping region. This condition is always satisfied for the parameters we explored in our simulations. When $w_{EE}/w_{EI} > w_{IE}/w_{II}$, region II amounts to $s_E > 0$ and $s_I < 0$ and the calculations are analogous. However, the flow can be reversed, so that a trajectory beginning in region II may cross to region I, and the latter becomes the trapping region instead.

-
- [1] J. Marro and R. Dickman, *Nonequilibrium Phase Transition in Lattice Models* (Cambridge University Press, Cambridge, 1999).
- [2] H. Hinrichsen, *Adv. Phys.* **49**, 815 (2000).
- [3] G. Grinstein and M. A. Muñoz, *The Statistical Mechanics of Absorbing States*, Lecture Notes in Physics, Vol. 493 (Springer, Berlin, 1997), p. 223.
- [4] M. Henkel, H. Hinrichsen, and S. Lübeck, *Non-Equilibrium Phase Transitions: Absorbing phase transitions*, Theoretical and Mathematical Physics (Springer, Berlin, 2008).
- [5] G. Ódor, *Universality in Nonequilibrium Lattice Systems: Theoretical Foundations* (World Scientific, Singapore, 2008).
- [6] H.-K. Janssen, *Z. Phys. B* **42**, 151 (1981).
- [7] P. Grassberger, in *Nonlinear Phenomena in Chemical Dynamics*, edited by C. Vidal and A. Pacault (Springer, Berlin, 1981), pp. 262–262.
- [8] J. Binney, N. Dowrick, A. Fisher, and M. Newman, *The Theory of Critical Phenomena* (Oxford University Press, Oxford, 1993).
- [9] M. A. Muñoz, G. Grinstein, R. Dickman, and R. Livi, *Phys. Rev. Lett.* **76**, 451 (1996).
- [10] G. Grinstein, Z.-W. Lai, and D. A. Browne, *Phys. Rev. A* **40**, 4820 (1989).
- [11] T. E. Harris, *The Theory of Branching Processes* (Courier Corporation, Berlin, 2002).
- [12] T. Liggett, *Interacting Particle Systems*, Classics in Mathematics (Springer, Berlin, 2004).

- [13] S. Lübeck, *J. Stat. Phys.* **123**, 193 (2006).
- [14] P. Villa Martín, J. A. Bonachela, and M. A. Muñoz, *Phys. Rev. E* **89**, 012145 (2014).
- [15] V. R. V. Assis and M. Copelli, *Phys. Rev. E* **80**, 061105 (2009).
- [16] J. M. Beggs and D. Plenz, *J. Neurosci.* **23**, 11167 (2003).
- [17] T. Mora and W. Bialek, *J. Stat. Phys.* **144**, 268 (2011).
- [18] D. R. Chialvo, *Nat. Phys.* **6**, 744 (2010).
- [19] M. A. Muñoz, *Rev. Mod. Phys.* **90**, 031001 (2018).
- [20] D. Plenz, T. L. Ribeiro, S. R. Miller, P. A. Kells, A. Vakili, and E. L. Capek, *Front. Phys.* **9**, 639389 (2021).
- [21] D. R. Chialvo, *Acta Phys. Pol. B* **49**, 1955 (2018).
- [22] J. O'Byrne *et al.*, *Trends Neurosci.* **45**, 820 (2022).
- [23] A. J. Fontenele, N. A. P. de Vasconcelos, T. Feliciano, L. A. A. Aguiar, C. Soares-Cunha, B. Coimbra, L. Dalla Porta, S. Ribeiro, A. J. Rodrigues, N. Sousa *et al.*, *Phys. Rev. Lett.* **122**, 208101 (2019).
- [24] A. Ponce-Alvarez, A. Jouary, M. Privat, G. Deco, and G. Sumbre, *Neuron* **100**, 1446 (2018).
- [25] D. Millman, S. Mihalas, A. Kirkwood, and E. Niebur, *Nat. Phys.* **6**, 801 (2010).
- [26] M. Martinello, J. Hidalgo, A. Maritan, S. di Santo, D. Plenz, and M. A. Muñoz, *Phys. Rev. X* **7**, 041071 (2017).
- [27] J. M. Cortes, M. Desroches, S. Rodrigues, R. Veltz, M. A. Muñoz, and T. J. Sejnowski, *Proc. Natl. Acad. Sci. USA* **110**, 16610 (2013).
- [28] M. Benayoun, J. D. Cowan, W. van Drongelen, and E. Wallace, *PLoS Comput. Biol.* **6**, e1000846 (2010).
- [29] O. Kinouchi and M. Copelli, *Nat. Phys.* **2**, 348 (2006).
- [30] M. Girardi-Schappo, E. F. Galera, T. T. Carvalho, L. Brochini, N. L. Kamiji, A. C. Roque, and O. Kinouchi, *J. Phys. Complex.* **2**, 045001 (2021).
- [31] M. Girardi-Schappo, L. Brochini, A. A. Costa, T. T. A. Carvalho, and O. Kinouchi, *Phys. Rev. Res.* **2**, 012042(R) (2020).
- [32] T. T. A. Carvalho, A. J. Fontenele, M. Girardi-Schappo, T. Feliciano, L. A. A. Aguiar, T. P. L. Silva, N. A. P. de Vasconcelos, P. V. Carelli, and M. Copelli, *Front. Neural Circuits* **14**, 576727(2021).
- [33] A. De Candia, A. Sarracino, I. Apicella, and L. de Arcangelis, *PLoS Comput. Biol.* **17**, e1008884 (2021).
- [34] M. K. Nandi, A. Sarracino, H. J. Herrmann, and L. de Arcangelis, *Phys. Rev. E* **106**, 024304 (2022).
- [35] I. Apicella, S. Scarpetta, L. de Arcangelis, A. Sarracino, and A. de Candia, *Sci. Rep.* **12**, 21870 (2022).
- [36] R. Corral López, V. Buendía, and M. A. Muñoz, *Phys. Rev. Res.* **4**, L042027 (2022).
- [37] H. R. Wilson and J. D. Cowan, *Biophys. J.* **12**, 1 (1972).
- [38] E. Wallace, M. Benayoun, W. van Drongelen, and J. D. Cowan, *PLoS ONE* **6**, 1 (2011).
- [39] Y. Maruyama, Y. Kakimoto, and O. Araki, *Biol. Cybern.* **108**, 355 (2014).
- [40] J. D. Cowan, J. Neuman, and W. van Drongelen, *J. Math. Neurosci.* **6**, 1 (2016).
- [41] F. C. Hoppensteadt and E. M. Izhikevich, *Weakly Connected Neural Networks*, Applied Mathematical Sciences, Vol. 126 (Springer, New York, 1997).
- [42] R. M. Borisyuk and A. B. Kirillov, *Biol. Cybern.* **66**, 319 (1992).
- [43] Let us remark that a very similar model has been recently proposed to generalize the standard contact process to include inhibitory units and is described by similar equations [36].
- [44] N. Brunel, *J. Comput. Neurosci.* **8**, 183 (2000).
- [45] N. V. Kampen, *Stochastic Processes in Physics and Chemistry* (North Holland, 2007).
- [46] C. W. Gardiner, *Handbook of Stochastic Methods for Physics, Chemistry and the Natural Sciences*, 3rd ed., Springer Series in Synergetics, Vol. 13 (Springer-Verlag, Berlin, 2004).
- [47] T. Ohira and J. D. Cowan, in *Mathematics of Neural Networks*, edited by S. W. Ellacott, J. C. Mason, and I. J. Anderson (Kluwer Academic Publishers, Norwell, 1997), pp. 290–294.
- [48] P. Glendinning and M. R. Jeffrey, *An Introduction to Piecewise Smooth Dynamics* (Birkhäuser, Cham, 2019).
- [49] J. Harris and B. Ermentrout, *SIAM J. Appl. Dyn. Syst.* **14**, 43 (2015).
- [50] M. Kunze, *Non-Smooth Dynamical Systems*, Lecture Notes in Mathematics, Vol. 1744 (Springer Science & Business Media, Berlin, 2000).
- [51] E. M. Izhikevich, *Dynamical Systems in Neuroscience* (MIT Press, Cambridge, 2007).
- [52] S. H. Strogatz, *Nonlinear Dynamics and Chaos with Student Solutions Manual: With Applications to Physics, Biology, Chemistry, and Engineering* (CRC Press, Boca Raton, 2018).
- [53] I. I. Lima Dias Pinto and M. Copelli, *Phys. Rev. E* **100**, 062416 (2019).
- [54] S. di Santo, P. Villegas, R. Burioni, and M. A. Muñoz, *J. Stat. Mech.* (2018) 073402.
- [55] M. A. Muñoz, R. Dickman, A. Vespignani, and S. Zapperi, *Phys. Rev. E* **59**, 6175 (1999).
- [56] J. Marro and R. Dickman, *Nonequilibrium Phase Transitions in Lattice Models*, Collection Alea-Saclay: Monographs and Texts in Statistical Physics (Cambridge University Press, Cambridge, 1999).
- [57] J. P. Sethna, K. A. Dahmen, and C. R. Myers, *Nature (London)* **410**, 242 (2001).
- [58] N. Friedman, S. Ito, B. A. W. Brinkman, M. Shimono, R. E. Lee DeVille, K. A. Dahmen, J. M. Beggs, and T. C. Butler, *Phys. Rev. Lett.* **108**, 208102 (2012).
- [59] S. di Santo, P. Villegas, R. Burioni, and M. A. Muñoz, *Phys. Rev. E* **95**, 032115 (2017).
- [60] N. Marshall, N. M. Timme, N. Bennett, M. Ripp, E. Lautzenhiser, and J. M. Beggs, *Front. Physiol.* **7**, (2016).
- [61] M. A. Muñoz, G. Grinstein, and Y. Tu, *Phys. Rev. E* **56**, 5101 (1997).
- [62] L. van Veen and M. Hoti, *Int. J. Bifurcation Chaos* **29**, 1950104 (2019).
- [63] L. Lai, Z. Zhu, and F. Chen, *Mathematics* **8**, 1280 (2020).
- [64] M. Fruchart, R. Hanai, P. B. Littlewood, and V. Vitelli, *Nature (London)* **592**, 363 (2021).
- [65] J. D. Noh and H. Park, *Phys. Rev. Lett.* **94**, 145702 (2005).
- [66] K. Christensen, H. C. Fogedby, and H. Jeldtoft Jensen, *J. Stat. Phys.* **63**, 653 (1991).
- [67] A. Chessa, H. E. Stanley, A. Vespignani, and S. Zapperi, *Phys. Rev. E* **59**, R12 (1999).
- [68] R. Dickman and J. M. M. Campelo, *Phys. Rev. E* **67**, 066111 (2003).
- [69] A. Deluca and Á. Corral, *Acta Geophysica* **61**, 1351 (2013).

- [70] S. Papanikolaou, F. Bohn, R. L. Sommer, G. Durin, S. Zapperi, and J. P. Sethna, *Nat. Phys.* **7**, 316 (2011).
- [71] S. R. Miller, S. Yu, and D. Plenz, *Sci. Rep.* **9**, 1 (2019).
- [72] L. Laurson, X. Illa, S. Santucci, K. Tore Tallakstad, K. J. Måløy, and M. J. Alava, *Nat. Commun.* **4**, 2927 (2013).
- [73] E. Gudowska-Nowak, M. A. Nowak, D. R. Chialvo, J. K. Ochab, and W. Tarnowski, *Neural Comput.* **32**, 395 (2020).
- [74] J. Hidalgo, L. Seoane, J. Cortés, and M. Muñoz, *PLoS ONE* **7**, e40710 (2012).
- [75] J. Almeida, T. S. Grigera, D. R. Chialvo, and S. A. Cannas, *Phys. Rev. E* **106**, 054140 (2022).
- [76] V. Buendía, P. Villegas, S. di Santo, A. Vezzani, R. Burioni, and M. A. Muñoz, *Sci. Rep.* **9**, 15183 (2019).
- [77] M. A. Muñoz, R. Juhász, C. Castellano, and G. Ódor, *Phys. Rev. Lett.* **105**, 128701 (2010).
- [78] P. Moretti and M. A. Muñoz, *Nat. Commun.* **4**, 2521 (2013).
- [79] G. Odor, *Phys. Rev. E* **94**, 062411 (2016).
- [80] D. T. Gillespie, *J. Comput. Phys.* **22**, 403 (1976).
- [81] D. T. Gillespie, *J. Phys. Chem.* **81**, 2340 (1977).